

Contents lists available at ScienceDirect

Journal of Computational Physics: X

www.elsevier.com/locate/jcpx



An improved discrete unified gas kinetic scheme for simulating compressible natural convection flows



Xin Wen^a, Lian-Ping Wang^{a,b,c,*}, Zhaoli Guo^d, Jie Shen^e

- ^a Department of Mechanical Engineering, 126 Spencer Laboratory, University of Delaware, Newark, DE 19716-3140, USA
- ^b Guangdong Provincial Key Laboratory of Turbulence Research and Applications, Center for Complex Flows and Soft Matter Research and Department of Mechanics and Aerospace Engineering, Southern University of Science and Technology, Shenzhen 518055, Guangdong, PR China
- ^c Guangdong-Hong Kong-Macao Joint Laboratory for Data-Driven Fluid Mechanics and Engineering Applications, Southern University of Science and Technology, Shenzhen 518055, China
- ^d State Key Laboratory of Coal Combustion, Huazhong University of Science and Technology, Wuhan, PR China
- ^e Shanghai Institute of Applied Mathematics and Mechanics, Shanghai University, Shanghai, PR China

ARTICLE INFO

Article history: Received 9 August 2020 Received in revised form 20 December 2020 Accepted 6 March 2021 Available online 16 March 2021

Keywords: Natural convection Compressible flow Boundary condition DUGKS

ABSTRACT

Discrete unified gas-kinetic scheme (DUGKS) has been developed recently as a general method for simulating flows at all Knudsen numbers. In this study, we extend DUGKS to simulate fully compressible thermal flows. We introduce a source term to the Boltzmann equation with the Bhatnagar-Gross-Krook (BGK) collision model [1] to adjust heat flux and thus the Prandtl number. The fully compressible Navier-Stokes equations can be recovered by the current model. As a mesoscopic CFD approach, it requires an accurate mesoscopic implementation of the boundary conditions. Using the Chapman-Enskog approximation, we derive the "bounce-back" expressions for both temperature and velocity distribution functions, which reveal the need to consider coupling terms between the velocity and thermal fields. To validate our scheme, we first reproduce the Boussinesq flow results by simulating natural convection in a square cavity with a small temperature difference ($\epsilon =$ 0.01) and a low Mach number. Then we perform simulations of steady natural convection $(Ra = 1.0 \times 10^6)$ in a square cavity with differentially heated side walls and a large temperature difference ($\epsilon = 0.6$), where the Boussinesq approximation becomes invalid. Temperature, velocity profiles, and Nusselt number distribution are obtained and compared with the benchmark results from the literature. Finally, the unsteady compressible natural convection with $Ra = 5.0 \times 10^9$, $\epsilon = 0.6$ is studied and the turbulent fluctuation statistics are computed and analyzed.

© 2021 The Author(s). Published by Elsevier Inc. This is an open access article under the CC BY-NC-ND license (http://creativecommons.org/licenses/by-nc-nd/4.0/).

1. Introduction

The buoyancy-driven natural convection in an enclosure, or internal natural convection, has been studied for a long time [2–4]. It plays an important role in both fundamental studies of thermal and velocity structures of buoyancy-driven flows and practical applications such as geophysics, astrophysics, solar energy collection devices, cooling of nuclear reactor or electronic equipment, energy storage systems, air conditioning systems, and food processing. The problem of internal natural convection can be roughly divided into two types. The first concerns enclosures heated from below, in which a temperature

E-mail address: wanglp@sustech.edu.cn (L.-P. Wang).

^{*} Corresponding author at: Department of Mechanics and Aerospace Engineering, Southern University of Science and Technology, Shenzhen, Guangdong 518055. China.

Table 1Studies of compressible natural convection.

	Method	Dimension & resolution	Α	Ra
Chenoweth [11]	FD	2D (121 × 121)	1 – 10	$10^3 - 10^7$
Quéré [13,26,27]	Spectral	2D $(80 \times 80, 32 \times 96)$	1, 8	$10^5, 10^6$
Vierendeels [14,15]	FV	2D (512 × 512)	1	$10^2 - 10^7$
Becker [28]	FE	2D $(4 \times 10^6 \text{ d.o.f})$	1	$10^6 - 10^7$
Li [19]	LBM	2D (250 × 250)	1	$10^3 - 10^5$
Feng [20,29]	LBM	2D $(100 \times 100 \times 10)$	1	$10^3 - 10^5$
Lenz [21]	GKS	2D (376 × 376)	1	$10^6, 5 \times 10^9$

gradient is parallel to the direction of gravity, such as the Rayleigh-Bérnard convection problem between two horizontal plates. The second type considers enclosures heated from side walls, in which the temperature gradient is orthogonal to the direction of gravity, like natural convection in differentially vertically heated enclosures (Pandey et al. 2019). Furthermore, based on the compressibility of the fluid, the buoyancy-driven natural convection can be classified into two categories: (1) Boussinesq flows when the temperature difference is small such that the flow can be assumed to be incompressible and the buoyancy effect can be represented by a linear function of the temperature; (2) non-Boussinesq flows when the temperature difference is large and the compressible effects must be considered and the fluid properties may also vary with temperature. In the latter case, the flow is governed by fully compressible Navier-Stokes-Fourier equations.

Led by the pioneering studies started in the 1970s [5,6], researchers have studied internal natural convection in both twoand three-dimensional cavities at different Rayleigh numbers and Prandtl numbers in different geometries. For example, using the pseudo-spectral method, Quéré [7] provided solutions for the full range of two-dimensional steady-state flow in a square cavity and concluded that the critical Rayleigh number for the transition from steady to unsteady flow is $Ra_{cr} = 1.82 \pm 0.01 \times 10^8$ [8]. Paolucci and Chenoweth [9] used the finite-difference method to solve this problem for Rayleigh number up to 10^{10} , and provided a detailed analysis of the influence of aspect ratio on the critical Rayleigh number. These studies were conducted under the Boussinesq approximation, where the density change is negligible except in the buoyancy term, and the fluid properties (viscosity, heat conductivity) are assumed to be constant.

However, for a differentially heated cavity with a large temperature difference, the Boussinesq approximation could become invalid, namely, the fluid properties could vary with temperature and expansion/contraction of fluid could become dynamically important. For these reasons, the temperature field and the velocity field are more strongly coupled for the compressible convection. While the nearly incompressible natural convection has been widely explored [4,10], there are very few studies of compressible natural convection with large temperature differences. Chenoweth and Paolucci [11] performed an early study of compressible natural convection. They provided two-dimensional steady-state results from the transient Navier-Stokes equations under the low Mach number approximation [12]. The governing equation they used is an approximation of the compressible Navier-Stokes equations, the total pressure is decomposed and only thermodynamic pressure is considered in the equation of state. Using a Chebyshev collocation algorithm, Quéré et al. [13] studied two-dimensional non-Boussinesq convection in a tall cavity with an aspect ratio (A = H/L) of 5, where H is the cavity height and L is the cavity length. They found that the flow become increasingly asymmetrical as the temperature difference is increased, and the critical Rayleigh number also decreases with larger temperature difference. Vierendeels et al. [14,15] solved twodimensional steady Navier-Stokes equations and provided solutions for the Rayleigh number $(Ra = Pr2\epsilon gH^3 \rho_0^2/\mu_0^2)$ ranging from $Ra = 10^2$ to $Ra = 10^7$ with a normalized temperature difference $\epsilon = (T_h - T_c)/2T_0$ at 0.6, where Pr is the Prandtl number, g is the gravity, ρ_0 is the density and μ_0 is viscosity at a reference temperature $T_0 = (T_h + T_c)/2$, respectively, T_h is the temperature of the hot wall and T_c is the temperature of the cold wall. They solved the compressible Navier-Stokes equations, however, as will be seen later in this paper, the steady flow assumption may not be valid for high Rayleigh number flows. Table 1 summarizes some representative works of compressible natural convection simulations. It is found that three-dimensional or unsteady compressible natural convection in an enclosure is rarely explored.

In recent years, mesoscopic methods based on model Boltzmann equations, such as the lattice Boltzmann method (LBM) and gas kinetic schemes, have been developed and applied to simulate both incompressible [16–18] and compressible [19–21] natural convection flows (also shown in Table 1). The mesoscopic methods solve a relatively simple governing equation and enjoy certain advantages such as low numerical dissipation, feasibility in treating complex boundaries, and high parallel efficiency. Different kinetic models have been proposed to treat non-Boussinesq thermal flow studies, in which the work done by viscous dissipation and compression are considered [22–25]. Among these approaches, the coupling double-distribution function model is widely employed in thermal flow simulations. The first DDF model that takes account of the viscous dissipation and compression work is proposed by He et al. [23]. An additional internal energy distribution function. However, in this method, the calculation of temperature involves the time and spatial derivative of the hydrodynamic variables which may introduce some errors. Later on, Guo et al. proposed an alternative thermal DDF model in which the viscous dissipation and compression work are also considered [25]. They employed a distribution function for the total energy rather than the internal energy in addition to the velocity distribution function. The introduction of the total energy distribution function avoids the spatial and time derivatives of the hydrodynamic variables. However, the model by Guo et al. assumes that the temperature variation is small and the flow is nearly incompressible. In the Hermite expansion of the

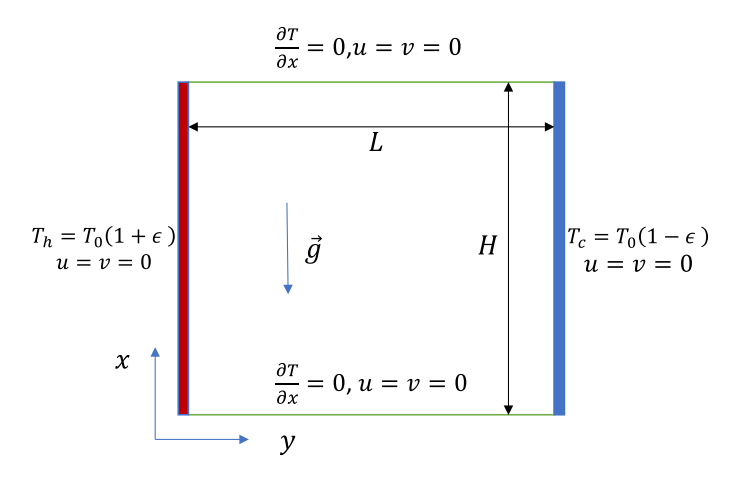


Fig. 1. The geometry under consideration.

equilibrium, the thermal part and the $\mathcal{O}(Ma^3)$ terms are neglected. Based on Guo's DDF model, some LBM models have been proposed later for the compressible case. The thermal parts are retained in the Hermite expansion of the equilibrium distribution. For example, Li et al. [19] used two coupled distribution functions in a lattice Boltzmann model to simulate steady compressible natural convection flow in a square cavity. Lenz et al. [21] reported results of two-dimensional unsteady compressible natural convection at $Ra = 5 \times 10^9$ using a gas-kinetic scheme, they did not make low Mach number assumption in their study and the finite-volume method allowed them to use non-uniform meshes near the wall.

The discrete unified gas-kinetic scheme (DUGKS) was recently developed by Guo et al. [30,31], combining the advantages of the unified gas kinetic scheme and LBM. DUGKS could be used to simulate different types of flows, from continuum to free molecular flows [32–35]. Wang et al. [18] simulated natural convection flows in a cavity under the Boussinesq approximation using two sets of distribution functions. Thermal flows with more complex geometries have also been studied by combining DUGKS with the immersed boundary method [36,37]. Due to the finite-volume formulation, non-uniform meshes can be easily employed in DUGKS [38], which is desired for simulating internal natural convection where thermal and velocity boundary layers are the essential flow features. Another advantage of DUGKS is that the boundary condition can be applied at the cell interface notes on the wall. The above studies considered only incompressible natural convection flows.

In this study, we will report first DUGKS simulations of compressible natural convection. In general, there are several issues in performing fully compressible natural convection simulations using DUGKS. The first is the ability to represent an arbitrary Prandtl number when the single-relaxation-time BGK collision model is used. This could be addressed by modifying the equilibrium distribution, such as in the BGK-Shakhov model [39] or ellipsoidal statistical model [40]. However, alteration of the equilibrium distribution could affect the order requirements of the Gauss-Hermite quadrature. Alternative approach is to add a properly designed source term to the energy distribution, as implied by the approach of Xu [41] who adjusted the macroscopic energy flux in their gas kinetic scheme. In Section 2, we re-visit the design of a source term in the evolution equation of the energy distribution, in order to adjust the heat flux and consequently the Prandtl number in a relatively simple manner.

Another important issue we wish to emphasize in this paper is the proper implementation of boundary conditions. For thermal flow simulations, both temperature and velocity boundary treatments are required, and the two are actually coupled in DUGKS of compressible convection. We will present a consistency approach to address this inherent complexity based on the Chapman-Enskog analysis.

The paper is organized as follows. In Sec. 2 and Appendix C, after presenting the physical problem and the kinetic scheme, we discuss a systematic derivation of the boundary conditions based on the Chapman-Enskog approximation. In Sec. 3, we first validate our revised DUGKS scheme by studying natural convection in a square cavity with a small temperature difference ($\epsilon = 0.01$) and compare our results with benchmark Boussinesq results from the literature. Then we investigate the compressible natural convection with a large temperature difference ($\epsilon = 0.6$) at a Rayleigh number $Ra = 1.0 \times 10^6$, again results will be compared with benchmark results. Finally, results of an unsteady compressible natural convection flow at $Ra = 5.0 \times 10^9$ and $\epsilon = 0.6$ will be presented. The main contributions and conclusions of this work are summarized in Sec. 4.

2. Governing equation and numerical methods

2.1. Problem description and governing equations

We consider a natural convection flow in a two-dimensional square cavity with a hot vertical wall $T_h = T_0(1 + \epsilon)$ on the left and a cold vertical wall $T_c = T_0(1 - \epsilon)$ on the right, while the top and bottom walls are adiabatic as shown in Fig. 1.

The current system is governed by the geometrical parameters (cavity height H, cavity length L), fluid properties (density ρ_0 , viscosity μ_0 , heat conductivity k_0 , heat capacity C_p , C_V), the temperature at the hot wall T_h and cold wall T_c . The governing equations can be written as:

$$\frac{\partial \rho}{\partial t} + \frac{\partial \left(\rho u_j\right)}{\partial x_j} = 0,\tag{1a}$$

$$\frac{\partial \left(\rho u_{i}\right)}{\partial t} + \frac{\partial \left(\rho u_{i} u_{j}\right)}{\partial x_{i}} = -\frac{\partial p}{\partial x_{i}} + \rho g_{i} + \frac{\partial \sigma_{ij}}{\partial x_{j}},\tag{1b}$$

$$\frac{\partial \left(\rho C_V T\right)}{\partial t} + \frac{\partial \left(\rho u_j C_V T\right)}{\partial x_j} = -p \frac{\partial u_j}{\partial x_j} + \frac{\partial}{\partial x_j} \left(k \frac{\partial T}{\partial x_j}\right) + \sigma_{ij} \frac{\partial u_j}{\partial x_j},\tag{1c}$$

$$p = \rho RT$$
, (1d)

where the stress tensor is $\sigma_{ij} = 2\mu \left(S_{ij} - \frac{1}{D}\nabla \cdot \boldsymbol{u}\delta_{ij}\right) + \mu^V \nabla \cdot \boldsymbol{u}\delta_{ij}$, S_{ij} is the strain rate tensor, μ and μ^V are the shear viscosity and the bulk viscosity, respectively. In order to normalize the system governing equations, we introduce a reference temperature $T_0 = (T_h + T_c)/2$, a reference density ρ_0 , and a reference viscosity $\mu_0 = \mu(T_0)$. The Mach number is defined as $Ma = u_0/c_s$, we choose buoyancy velocity $u_0 = \sqrt{(T_h - T_c)gH/T_0}$ as reference velocity and speed of sound is $c_s = \sqrt{\gamma RT_0}$. When the temperature difference is large, the fluid properties are temperature dependent, the viscosity and heat conductivity are given by Sutherland's law:

$$\frac{\mu(T)}{\mu^*} = \left(\frac{T}{T^*}\right)^{3/2} \frac{T^* + S}{T + S}, \quad k(T) = \frac{\mu(T) C_p}{Pr},\tag{2}$$

where $T^* = 273$ K and S = 110.5 K. The viscosity at a reference temperature T_0 , $\mu_0 = \mu(T_0)$, is then calculated by $\mu^* = \mu_0 \left[\left(\frac{T_0}{T^*} \right)^{3/2} \frac{T^* + S}{T + S} \right]^{-1}$. The continuity equation and the momentum equation are then normalized by using the density scale

 ρ_0 , the velocity scale u_0 , length scale H, and time scale H/u_0 ; the pressure is normalized by $\rho_0 u_0^2$; the viscous stress is normalized by $\mu_0 u_0/H$. The energy equation is normalized by using the temperature scale T_0 , density scale ρ_0 , and the same velocity and time scales; the conductivity is normalized by $k_0 \equiv k(T_0)$. The dimensionless governing equations of compressible natural convection can be written as:

$$\frac{\partial \hat{\rho}}{\partial \hat{t}} + \frac{\partial \left(\hat{\rho}\hat{u}_{j}\right)}{\partial \hat{x}_{i}} = 0, \tag{3a}$$

$$\frac{\partial \left(\hat{\rho}\hat{u}_{i}\right)}{\partial \hat{t}} + \frac{\partial \left(\hat{\rho}\hat{u}_{i}\hat{u}_{j}\right)}{\partial \hat{x}_{i}} = -\frac{\partial \hat{p}}{\partial \hat{x}_{i}} + \frac{1}{2\epsilon}\hat{\rho}\delta_{i1} + \sqrt{\frac{Pr}{Ra}}\frac{\partial \hat{\sigma}_{ij}}{\partial \hat{x}_{j}},\tag{3b}$$

$$\frac{\partial \left(\hat{\rho}\hat{T}\right)}{\partial \hat{t}} + \frac{\partial \left(\hat{\rho}\hat{u}_{j}\hat{T}\right)}{\partial \hat{x}_{j}} = \Lambda \left[-\hat{p}\frac{\partial \hat{u}_{j}}{\partial \hat{x}_{j}} + \frac{\gamma}{\Lambda\sqrt{RaPr}}\frac{\partial}{\partial \hat{x}_{j}}\left(k\frac{\partial \hat{T}}{\partial \hat{x}_{j}}\right) + \sqrt{\frac{Pr}{Ra}}\hat{\sigma}_{ij}\frac{\partial \hat{u}_{j}}{\partial \hat{x}_{j}}\right],\tag{3c}$$

where $\Lambda = \gamma \ (\gamma - 1) \ Ma^2$, and the x axis is assumed to be in the upward vertical direction. The above dimensionless governing equations indicate that there are four dimensionless governing parameters: Rayleigh number Ra, Prandtl number $Pr = \mu_0 C_p / k_0$, Mach number Ra, and heat capacity ratio $\gamma = C_p / C_V$. The geometry and boundary conditions introduce two additional parameters: the aspect ratio A = H/L and the relative temperature difference ϵ . The controlling parameters for the current problem are the Rayleigh number Ra and the relative temperature difference ϵ :

$$Ra = \frac{Pr2\epsilon gH^{3}\rho_{0}^{2}}{\mu_{0}^{2}}, \quad \epsilon = \frac{T_{h} - T_{c}}{2T_{0}}.$$
 (4)

For an air-filled square cavity, the Prandtl number Pr = 0.71 and heat capacity ratio $\gamma = 1.4$ are fixed.

The above equations represent a fully compressible, time-dependent thermal flow system, no Boussinesq approximation or low Mach number assumption is made. This allows us to treat both Boussinesq flow and compressible natural convection. Transient behaviors can also be analyzed for high Rayleigh number cases.

2.2. The kinetic model

The above hydrodynamic equations can be recovered through a kinetic model based on a model Boltzmann equation. We follow the Boltzmann equation with the Bhatnagar-Gross-Krook (BGK) collision model [1] used in Guo [31], namely,

$$\frac{\partial f}{\partial t} + \boldsymbol{\xi} \cdot \nabla_{\boldsymbol{x}} f + \boldsymbol{b} \cdot \nabla_{\boldsymbol{\xi}} f = -\frac{f - f^{eq}}{\tau} + S_f, \tag{5}$$

where $f(\mathbf{x}, \boldsymbol{\xi}, \boldsymbol{\eta}, \boldsymbol{\zeta}, t)$ is distribution function describing the motion of particles at the location $\mathbf{x} = (x_1, ..., x_D)$ and time t with microscopic velocity $\boldsymbol{\xi} = (\xi_1, ..., \xi_D)$, where D is the spatial dimension of the hydrodynamic velocity u_i . The remaining (3-D) space of the microscopic velocity is denoted by $\boldsymbol{\eta}$. Furthermore, an internal kinetic variable, $\boldsymbol{\zeta}$, of dimension K is introduced in order to adjust the specific heat ratio of the model. The external force per unit mass is given by \boldsymbol{b} , and τ is the relaxation time. The Maxwellian equilibrium is given as:

$$f^{eq} = \frac{\rho}{(2\pi RT)^{(3+K)/2}} \exp\left(-\frac{c^2 + \eta^2 + \zeta^2}{2RT}\right),\tag{6}$$

where $c \equiv \xi - u$ is the peculiar velocity. The hydrodynamic (conservative) flow variables can be obtained by the moments of the distribution function:

$$\rho = \int f d\xi d\eta d\zeta, \quad \rho \mathbf{u} = \int \xi f d\xi d\eta d\zeta, \quad \rho E = \int \frac{\xi^2 + \eta^2 + \zeta^2}{2} f d\xi d\eta d\zeta, \tag{7}$$

and the Maxwellian equilibrium implies that $\rho E = \rho u^2/2 + \rho c_V T$ with $c_V = (3 + K)R/2$ being the specific heat capacity at constant volume. The specific heat ratio for the model is $\gamma = (5 + K)/(3 + K)$, yielding the specific heat ratio of the air $\gamma = 1.4$ when K = 2.

One problem with the BGK collision model is that it would lead to a unit Prandtl number if the source term S_f is not present. There are multiple solutions for this problem. One way is to modify the equilibrium distribution, such as in the BGK-Shakov model [39] and the ellipsoidal statistical model [40]. However, this approach could affect the minimum order requirement for the Gauss-Hermite quadrature used to compute the moments of the distribution function in numerical implementation of the model. For instance, based on the Chapman-Enskog approximation as discussed in Shan et al. [42], heat flux calculation requires an evaluation of the fourth-order moment of the Maxwellian equilibrium distribution in the original model. If the BGK-Shakhov model is used as in Guo et al. [31], then heat flux calculation would require an evaluation of the six-order moment of the Maxwellian equilibrium distribution instead, due to the added prefactor in the BGK-Shakhov equilibrium distribution. This implies that the original requirement of a minimum eighth order Gauss-Hermite quadrature is transformed to a new requirement of twelfth order Gauss-Hermite quadrature. To avoid this dramatic increase in the quadrature order, we instead keep the equilibrium distribution untouched, but add a properly-designed source term S_f whose only purpose is to alter the resulting heat flux of the system. While, in principal, the two approaches to modify the Prandtl number are formally the same at the continuous Boltzmann equation level, they differ in the numerical implementations using discrete particle velocities. A higher quadrature order requires a larger number of discrete particle velocities, which we choose to avoid here. The source term S_f is designed as:

$$S_f = \tilde{\omega} \left[\frac{\eta^2 + \zeta^2}{(K + 3 - D)RT_0} - 1 \right] \frac{(1 - Pr)q_i \xi_i}{\tau (\sqrt{RT_0})^{4 - D}},\tag{8}$$

where $\tilde{\omega}(\xi, \eta, \zeta) = \frac{1}{(\sqrt{2\pi RT_0})^{K+3}} \exp\left(-\frac{\xi^2 + \eta^2 + \zeta^2}{2RT_0}\right)$ is the weighting function, and q_i is the heat flux which is related to the distribution function by

$$q_{i} = \frac{1}{2} \int c_{i}(c^{2} + \eta^{2} + \zeta^{2}) f d\xi d\eta d\zeta.$$
(9)

Note that the source term satisfies the following design constraints

$$\int S_f d\xi d\eta d\zeta = 0, \quad \int \xi_i S_f d\xi d\eta d\zeta = 0, \quad \int \xi_i \xi_j S_f d\xi d\eta d\zeta = 0, \tag{10a}$$

$$\int \frac{\left(\xi^2 + \eta^2 + \zeta^2\right)}{2} S_f d\xi d\eta d\zeta = 0, \quad \int \frac{c_i(c^2 + \zeta^2 + \eta^2)}{2} \tau S_f = (1 - Pr)q_i. \tag{10b}$$

Since these constraints are in integral form so the design is not unique. The explicit form of S_f given above is just one of the many possible forms. For our study here, we have D=3 and K=2. We note that for the very specific case of K=0 and D=3, the above source term is no longer suitable. For this case, there are alternative designs as explained in Chen et al. [43].

For efficient numerical implementation, it is more convenient to first integrate out the inactive degree of freedoms (η, ζ) , by introducing two reduced distributions $g(\mathbf{x}, \xi, t)$ and $h(\mathbf{x}, \xi, t)$ [31]:

$$g(\mathbf{x}, \boldsymbol{\xi}, t) = \int f(\mathbf{x}, \boldsymbol{\xi}, \boldsymbol{\eta}, \boldsymbol{\zeta}, t) d\boldsymbol{\eta} d\boldsymbol{\zeta}, \tag{11a}$$

$$h(\mathbf{x}, \boldsymbol{\xi}, t) = \int \left(\eta^2 + \zeta^2\right) f(\mathbf{x}, \boldsymbol{\xi}, \boldsymbol{\eta}, \boldsymbol{\zeta}, t) d\boldsymbol{\eta} d\boldsymbol{\zeta}. \tag{11b}$$

Correspondingly, the governing equations for $g(\mathbf{x}, \boldsymbol{\xi}, t)$ and $h(\mathbf{x}, \boldsymbol{\xi}, t)$ can be obtained from Eq. (5) as:

$$\frac{\partial g}{\partial t} + \boldsymbol{\xi} \cdot \nabla_{\mathbf{x}} g + \boldsymbol{b} \cdot \nabla_{\boldsymbol{\xi}} g = \Omega_g = -\frac{g - g^{eq}}{\tau},\tag{12a}$$

$$\frac{\partial h}{\partial t} + \boldsymbol{\xi} \cdot \nabla_{\boldsymbol{x}} h + \boldsymbol{b} \cdot \nabla_{\boldsymbol{\xi}} h = \Omega_h = -\frac{h - h^{eq}}{\tau} + S_h, \tag{12b}$$

where the reduced equilibriums g^{eq} and h^{eq} are

$$g^{eq} = \int f^{eq} d\eta d\zeta = \frac{\rho}{(2\pi RT)^{D/2}} \exp\left[-\frac{(\boldsymbol{\xi} - \boldsymbol{u})^2}{2RT}\right],\tag{13a}$$

$$h^{eq} = \int \left(\eta^2 + \zeta^2\right) f^{eq} d\eta d\zeta = (K + 3 - D) RT g^{eq}. \tag{13b}$$

It follows from Eq. (7) that the hydrodynamic variables should be computed as

$$\rho = \int g d\xi, \quad \rho \mathbf{u} = \int \xi g d\xi, \quad \rho E = \frac{1}{2} \int \left(\xi^2 g + h \right) d\xi. \tag{14}$$

And the source term makes zero contribution to the g evolution equation and

$$S_h = \int (\eta^2 + \zeta^2) S_f d\eta d\zeta = \omega(\xi) \frac{2(1 - Pr)q_i}{\tau \sqrt{RT_0}} \frac{\xi_i}{\sqrt{RT_0}},\tag{15}$$

where $\omega(\xi) = \frac{1}{(\sqrt{2\pi R T_0})^D} \exp\left(-\frac{\xi^2}{2R T_0}\right)$ is the weighting function. The source term S_h contributes to the first order momentum of h, which affects the resulting heat flux $q_i = \frac{1}{2} \int c_i(c^2g + h)d\xi$. Thus, it is sufficient to have the 1st order Hermite polynomial $\frac{\xi_i}{\sqrt{RT_0}}$ in the S_i . The detailed derivation for the design of the source term is presented in Appendix B.

It is important to point out that the two reduced distributions are not independent for compressible flow, the velocity field is highly coupled with the temperature field. In the current system of two reduced distributions, the temperature field is determined by g and h together. As the evolution equations Eq. (12a) and (12b) for g and h have the same form, we then use ϕ to represent g or h. As we do not have the explicit solution of ϕ , an approximation of the forcing term $\mathbf{b} \cdot \nabla_{\xi} \phi$ is needed. The Chapman-Enskog approximation implies that, for continuum flow, the forcing term can be approximated as:

$$F_{\phi} = -\mathbf{b} \cdot \nabla_{\xi} \phi \approx -\mathbf{b} \cdot \nabla_{\xi} \phi^{eq} = \frac{\mathbf{b} \cdot (\xi - \mathbf{u})}{RT} \phi^{eq}. \tag{16}$$

2.3. The DUGKS algorithm

The full DUGKS can be constructed based on the reduced governing equations Eq. (12a) and (12b) with approximated forcing term [18], we combine the forcing term F_{ϕ} with collision term Ω_{ϕ} , and denote it as $\bar{\Omega}_{\phi}$ which no longer conserves momentum and energy as shown in Eq. (18):

$$\frac{\partial \phi}{\partial t} + \xi \cdot \nabla_{\mathbf{x}} \phi = \bar{\Omega}_{\phi} = \Omega_{\phi} + F_{\phi}, \tag{17}$$

$$\int \boldsymbol{\xi} \bar{\Omega}_{g} d\boldsymbol{\xi} = \rho \boldsymbol{b}, \quad \int \left(\xi^{2} \bar{\Omega}_{g} + \bar{\Omega}_{h} \right) d\boldsymbol{\xi} = 2\rho \boldsymbol{u} \boldsymbol{b}. \tag{18}$$

As a finite-volume method, the first step is to decompose the computational domain into a set of control volumes. Eq. (17) is integrated over a cell V_j located at \mathbf{x}_j from time t_n to t_{n+1} . The mid-point rule is used for the convection term and the trapezoidal rule is applied to the collision term, then the equation can be written as:

$$\tilde{\phi}_{j}^{n+1} = \tilde{\phi}_{j}^{+,n} - \frac{\Delta t}{|V_{j}|} F^{n+\frac{1}{2}}, \quad F^{n+\frac{1}{2}} = \int_{\partial V_{j}} (\boldsymbol{\xi} \cdot \boldsymbol{n}) \, \phi \left(\boldsymbol{\xi}, \boldsymbol{x}, t_{n+1/2} \right) d\boldsymbol{S}, \tag{19}$$

where the time implicity has been removed by defining

$$\tilde{\phi} = \phi - \frac{\Delta t}{2} \bar{\Omega}_{\phi}, \quad \tilde{\phi}^{+} = \phi + \frac{\Delta t}{2} \bar{\Omega}_{\phi}, \tag{20}$$

and they are understood as cell-averaged values, $F^{n+\frac{1}{2}}$ is microscopic flux across the cell interface and \boldsymbol{n} is the outward unit vector normal to cell interface \boldsymbol{x}_b and $t_{n+1/2} \equiv t_n + 0.5 \Delta t$.

Table 2Gauss-Hermite quadrature formula D2Q25.

Quadrature	ξ _a	W_a	р	
D2Q25	(0,0)	64/225	1	$r^2 = 5 + \sqrt{10}$
	$(\pm r, 0)$	$2(7-2\sqrt{10})/225$	4	$r^2 = 5 - \sqrt{10}$
	$(\pm s, 0)$	$2(7+2\sqrt{10})/225$	4	
	$(\pm r, \pm r)$	$(89 - 28\sqrt{10})/3600$	4	
	$(\pm s, \pm s)$	$(89 + 28\sqrt{10})/3600$	4	
	$(\pm r, \pm s)$	1/400	8	

All hydrodynamic variables can be obtained from the auxiliary distribution $\tilde{\phi}$ directly. For the evolution of Eq. (19), the key point is to evaluate the microscopic flux $F^{n+\frac{1}{2}}$ at the cell interface at half time step which requires the reconstruction of the original distribution $\phi\left(\xi, \mathbf{x}_b, t_{n+1/2}\right)$. In order to do that, we integrate the Boltzmann equation Eq. (17) with a half time step $h = \frac{\Delta t}{2}$ along the characteristic line with end point at the cell interface \mathbf{x}_b , again trapezoidal rule is applied on the collision term:

$$\phi\left(\boldsymbol{\xi}, \boldsymbol{x}_{b}, t_{n+1/2}\right) - \phi\left(\boldsymbol{\xi}, \boldsymbol{x}_{b} - \boldsymbol{\xi}h, t_{n}\right) = \frac{h}{2} \left[\bar{\Omega}_{\phi}\left(\boldsymbol{\xi}, \boldsymbol{x}_{b}, t_{n+1/2}\right) + \bar{\Omega}_{\phi}\left(\boldsymbol{\xi}, \boldsymbol{x}_{b} - \boldsymbol{\xi}h, t_{n}\right)\right]. \tag{21}$$

Once again to remove time implicity, another two auxiliary distributions $\bar{\phi} = \phi - \frac{h}{2}\bar{\Omega}_{\phi}$ and $\bar{\phi}^+ = \phi + \frac{h}{2}\bar{\Omega}_{\phi}$ are introduced. And Taylor expansion around the node (ξ, \mathbf{x}_b, t_n) is applied to $\bar{\phi}^+(\xi, \mathbf{x}_b - \xi h, t_n)$:

$$\bar{\phi}\left(\boldsymbol{\xi}, \boldsymbol{x}_h, t_{n+1/2}\right) = \bar{\phi}^+\left(\boldsymbol{\xi}, \boldsymbol{x}_h - \boldsymbol{\xi}h, t_n\right) = \bar{\phi}^+\left(\boldsymbol{\xi}, \boldsymbol{x}_h, t_n\right) - \boldsymbol{\xi}h \cdot \boldsymbol{\sigma}_h,\tag{22}$$

where $\sigma_b = \nabla_{\mathbf{x}}\bar{\phi}^+(\boldsymbol{\xi},\mathbf{x}_b,t_n)$. It is obvious that the right-hand side of the Eq. (22) is explicit, $\bar{\phi}^+$ can be obtained by interpolation and the slope σ_b can be estimated from the difference between the two neighboring cells for smooth flows. Hydrodynamic variables at time $t_{n+1/2}$ can be computed from distribution function $\bar{\phi}(\boldsymbol{\xi},\mathbf{x}_b,t_{n+1/2})$. Then the equilibrium ϕ^{eq} can be obtained and the original distribution can be extracted from $\bar{\phi}$:

$$\phi\left(\xi, \mathbf{x}_{b}, t_{n+1/2}\right) = \frac{2\tau}{2\tau + h} \bar{\phi}\left(\xi, \mathbf{x}_{b}, t_{n+1/2}\right) + \frac{h}{2\tau + h} \phi^{eq}\left(\xi, \mathbf{x}_{b}, t_{n+1/2}\right) + \frac{\tau h}{2\tau + h} F_{\phi}. \tag{23}$$

With the original distribution $\phi\left(\boldsymbol{\xi}, \boldsymbol{x}_b, t_{n+1/2}\right)$ computed at the cell interface \boldsymbol{x}_b at time $t_{n+1/2}$, the microscopic flux $F^{n+\frac{1}{2}}$ can be obtained and this complete the whole evolution process. The current scheme is valid for continuum flow due to our treatment of the forcing term, the compressible Navier-Stokes equation can be recovered with the following transport properties before normalization

$$\mu = p\tau, \ \mu^{V} = \left(\frac{2}{D} - \frac{2}{K+3}\right)p\tau, \ k = \frac{\mu C_p}{Pr} = \frac{p\tau}{Pr} \frac{(K+5)R}{2}.$$
 (24)

In the numerical implementation, the equilibrium distribution is approximated by its fourth-order Hermite expansion as shown in Appendix A, we use D2Q25 discrete particle velocity model which has the 9^{th} -order algebraic degree of precision (Table 2).

2.4. Kinetic treatment of boundary conditions

For our problem, we have no-slip velocity condition on all walls, and there are two types of temperature boundary conditions: adiabatic wall of zero heat flux and isothermal wall of constant temperature. The velocity field is determined by distribution $g(\xi, \mathbf{x}, t)$ while the temperature field is controlled by both $g(\xi, \mathbf{x}, t)$ and $h(\xi, \mathbf{x}, t)$ together, thus it is more complex to perform the kinetic treatment (i.e., in terms of g and h) of the boundary conditions. In Appendix C, we show how to relate a pair of distributions with opposite particle velocities, and such relations are used to perform the kinetic boundary-condition treatment. First, the no-slip velocity condition is accomplished by the following relation derived in Appendix C:

$$g(\xi_{a,j}) = g(\xi_{\bar{a},j}) - \tau W_{a} \rho_{w} \frac{\xi_{a,j}}{T_{0}} \frac{\partial T}{\partial x_{j}} \begin{cases} \left(\frac{\xi_{a}^{2}}{RT_{0}} - D - 2\right) \\ \frac{1}{2}(\theta - 1) \left[\frac{\xi_{a}^{4}}{(RT_{0})^{2}} - 2(D + 3)\frac{\xi_{a}^{2}}{RT_{0}} + (D + 2)^{2}\right] \\ \frac{1}{8}(\theta - 1)^{2} \left[\frac{\xi_{a}^{6}}{(RT_{0})^{3}} - (3D + 14)\frac{\xi_{a}^{4}}{(RT_{0})^{2}} + (D + 4)(3D + 10)\frac{\xi_{a}^{2}}{(RT_{0})} + (D + 2)^{2}(D + 4) \right] \\ + \mathcal{O}(\tau^{2}, Ma^{5}), \end{cases}$$

$$(25)$$

where ξ_a and W_a are the abscissas and the corresponding weights of the chosen quadrature. θ is the normalized temperature defined as $\theta = \frac{T_w}{T_0}$. ρ_w , T_w are density, temperature at the wall, $\xi_{a,j}$ denote the particles bouncing back from the wall and $\xi_{\bar{a},j} = -\xi_{a,j}$. The above boundary condition may be viewed as corrected or improved bounce-back rule retaining $\mathcal{O}(\tau)$ terms due to the velocity-temperature coupling. For an isothermal flow, this recovers the standard bounce-back implementation. For an adiabatic wall, temperature gradient in the wall normal direction is zero $\frac{\partial T}{\partial x} = 0$. Temperature gradients in the tangential direction are approximated from the temperature values at the previous time step by finite-difference. For isothermal wall, $T_w = T_h$ or $T_w = T_c$ is applied, then the temperature gradient in tangential direction is zero. Temperature gradients in wall normal direction are approximated with values at the previous time step by finite-difference.

Next, we consider the adiabatic thermal boundary. The bounce back relation in this case reads

$$h(\xi_{a,j}) = h(\xi_{\bar{a},j}) - \tilde{K}\rho R\tau W_a \xi_{a,j} \frac{\partial T}{\partial x_j} \left\{ \left(\frac{\xi_a^2}{RT_0} - D \right) + \frac{1}{2} (\theta - 1) \left[\frac{\xi_a^4}{(RT_0)^2} - 2(D+1) \frac{\xi_a^2}{RT_0} + D^2 \right] \right\} + 2W_a \frac{2(1-Pr)}{\sqrt{RT_0}} \frac{\xi_a \cdot \mathbf{q}}{\sqrt{RT_0}} + \mathcal{O}(\tau^2, Ma^3),$$
(26)

where $\tilde{K} \equiv (K+3-D)$. $q_X=0$ and $\frac{\partial T_w}{\partial x}=0$ are imposed on the top and bottom walls. Heat flux in tangential direction q_y can be approximated by the heat flux value at previous time step $q_y^{(n-1)}=\frac{1}{2}\int c_y(c^2g^{(n-1)}+h^{(n-1)})d\xi$. Temperature gradient in the tangential direction is also calculated by the values from the last time step by finite difference.

Finally, for an isothermal wall, anti-bounce back is used for $h(\xi, \mathbf{x}, t)$:

$$h(\xi_{a,j}) = -h(\xi_{\tilde{a},j}) + 2W_{a}\tilde{K}p \left[1 + \frac{1}{2} (\theta - 1) \left(\frac{\xi_{a}^{2}}{RT_{0}} - D \right) \right]$$

$$+ 2\tau W_{a}\tilde{K}p \frac{\partial u_{j}}{\partial x_{j}} \left[(2 - \theta) \frac{\xi_{a}^{2}}{(K+3)RT_{0}} + \frac{\tilde{K}+2}{K+3} + \frac{1}{2} (\theta - 1) \left(\frac{\xi_{a}^{2}}{RT_{0}} - D \right) \left(\frac{\xi_{a}^{2}}{(K+3)RT_{0}} + \frac{\tilde{K}+2}{K+3} \right) \right]$$

$$+ 2\tau W_{a}\tilde{K}p \frac{\xi_{a,i}\xi_{a,j}}{RT_{0}} \frac{\partial u_{i}}{\partial x_{j}} \left[\theta - 2 - \frac{1}{2} (\theta - 1) \left(\frac{\xi_{a}^{2}}{RT_{0}} - D \right) \right] + \mathcal{O}(\tau^{2}, Ma^{3}),$$

$$(27)$$

where $T_W = T_h$ or $T_W = T_c$ is applied at hot and cold wall respectively. As the no-slip boundary condition is enforced, the velocity gradients $\frac{\partial \mathbf{u}}{\partial x} = 0$ are zero. The velocity gradients $\frac{\partial \mathbf{u}}{\partial y}$ are approximated from velocities values at previous time step by finite-difference.

All the above relations are derived based on the Chapman-Enskog approximation and have an accuracy up to $\mathcal{O}(\tau)$, which is consistent with compressible Navier-Stokes and energy equations. The derivation details are presented in Appendix C. It is worth pointing out that the boundary condition treatments we derived above are based on the kinetic model and the physical boundary conditions. The methodology of deriving kinetic boundary conditions based on Chapman-Enskog analysis can be applied to other kinetic models, such as LBM, to improve the local accuracy of a kinetic method near the boundary.

Table 3Parameters for the simulation of natural convection with a small temperature difference.

Ra	Pr	γ	ϵ	Ма	$p_0 (\mathrm{kg/m} \mathrm{s}^2)$	T_0 (K)	$R (m^2/s^2 K)$	$g \ (m/s^2)$	μ_0
1.0×10^{6}	0.71	1.4	0.01	4.108×10^{-3}	101325.0	600.0	287	g(Ra)	0.001

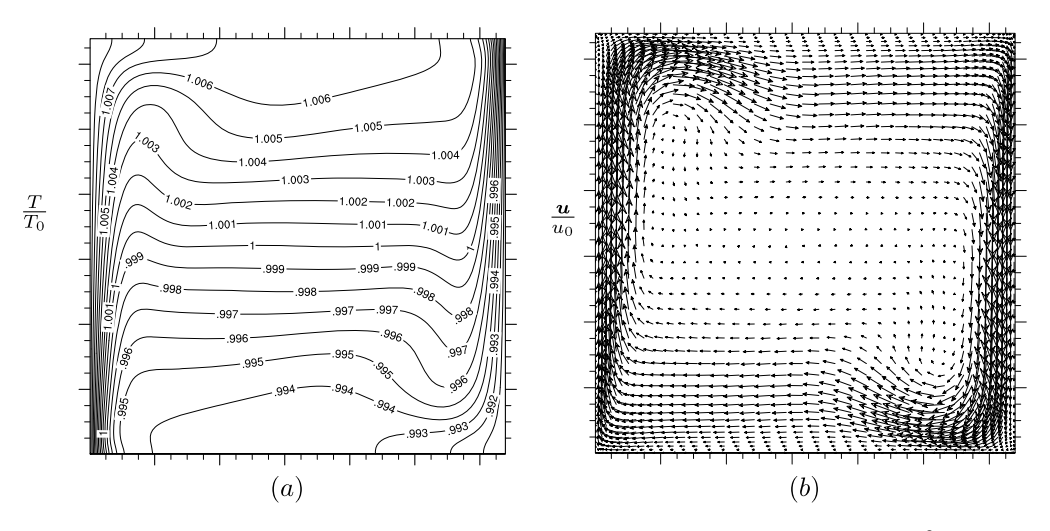


Fig. 2. (a). Isotherms; (b). Velocity vector plot for nearly incompressible natural convection with $Ra = 1.0 \times 10^6$, $\epsilon = 0.01$.

3. Results and discussion

3.1. The Boussinesq case

The current scheme is capable of simulating both compressible and incompressible natural convections as the governing equations we use are fully compressible Navier-Stokes and energy equations. To validate the code, we first perform a simulation of natural convection in an air-filled square cavity with a small temperature difference and a low Mach number ($\epsilon \ll 1$, $Ma \ll 1$), the Boussinesq results should be reproduced. Table 3 shows the parameter setting of the simulation, with a small temperature difference the fluid properties can be treated as constants. Non-uniform meshes 128 \times 128 are used in both horizontal and vertical directions.

Besides small temperature difference, to reproduce the Boussinesq results with compressible Navier-Stokes equation, a low Mach number is also required. However, a small Mach number leads to enormous computational cost due to the CFL restriction, a compromise between small Mach number and computational cost is needed. Initially, the fluid is quiescent u = 0 and isothermal $T = T_0$.

Fig. 2 shows the isotherms and velocity vector plot of nearly incompressible natural convection. Driven by the buoyancy force, the temperature boundary layer and the velocity boundary layer are developed along the isothermal walls. We can observe that there is temperature stratification in the core region, the flow field is symmetrical about the cavity center. All the characteristic flow features of Boussinesq flow are reproduced. Besides the instantaneous flow field, we also provide a detailed comparison of temperature and velocity profiles.

Temperature profiles and velocity profiles at mid-height and mid-width of the cavity are shown in Fig. 3, and are compared to the Boussinesq results of the Wang et al. [18] using the DUGKS for Boussinesq flows, the finite-difference results of Fusegi et al. [44] and experimental results of Bilski et al. [45]. It is obvious that our compressible scheme can nicely reproduce the Boussinesq results.

In Table 4 we compare results of the maximum vertical/horizontal velocities $(\frac{u_{max}}{u_0}, \frac{v_{max}}{u_0})$ and their horizontal/vertical locations $(\frac{y}{H}, \frac{x}{H})$ with the results under the Boussinesq assumption using other numerical methods. Clearly, our results agree well with the reference solutions. Therefore, we can claim that our compressible solver successfully reproduces the Boussinesq results when the temperature difference is small.

3.2. Compressible steady natural convection

After validating our scheme with nearly incompressible natural convection, we move to simulate steady compressible natural convection. Table 5 shows the parameter setting of natural convection with a large temperature difference at $\epsilon=0.6$ and Rayleigh number $Ra=1.0\times 10^6$. The left wall of the cavity is fixed at a high temperature of $T_h=0.6$ 0 K and the right wall is kept at a low temperature of $T_c=0.6$ 1 K. With this large temperature variance, the Boussinesq assumption is no longer valid. The density and the fluid properties vary with the temperature, the maximal density ratio is $\rho_{max}/\rho_{min}=0.0$ 1.

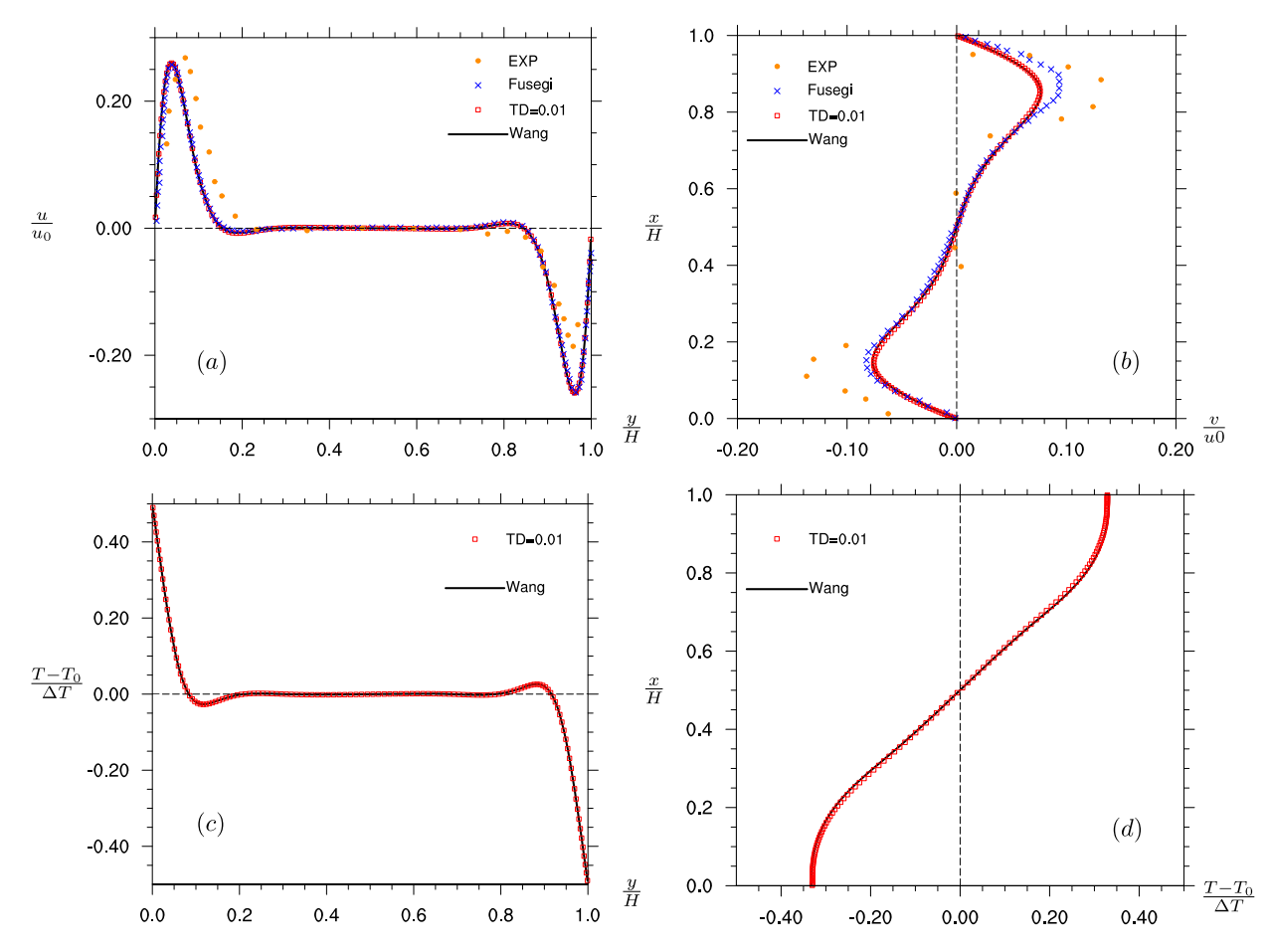


Fig. 3. (*a*) Vertical velocity u/u_0 and (*c*) Temperature distribution at the mid-height x = 0.5H; (*b*) Horizontal velocity v/u_0 and (*d*) Temperature distribution at the mid-width y = 0.5H for $Ra = 1.0 \times 10^6$, $\epsilon = 0.01$.

Table 4 Characteristic values comparison, $Ra = 1.0 \times 10^6$, $\epsilon = 0.01$.

	Present	DUGKS [18]	FD [46]	Spectral [47]
u_{max}/u_0	0.2599	0.2588	0.2603	0.2617
y/H	0.0383	0.0391	0.0379	0.038
v_{max}/u_0	0.0758	0.0757	0.0767	0.077
x/H	0.8546	0.8594	0.850	0.841
Nu_o	8.83	8.679	8.80	8.82

as shown in Fig. 4(a). For this case, both the thermal boundary layer and the velocity boundary layer of the cold wall are expected to be thin, thus fine meshes are needed near the wall. A non-uniform grid with a resolution of 256×256 is used, where the minimum grid space near the wall is of the length $\Delta x_{min} = 2.683 \times 10^{-4} H$. The CFL number in the current simulation is 0.5. The code was run on the National Center for Atmospheric Research's (NCAR-Wyoming) Supercomputer, known as Cheyenne, equipped with 2.3-GHz Intel Xeon E5-2697V4 processors. The computational domain are decomposed in the y, 128 processors are employed for the current case. The wall clock time per step is $1.86 \times 10^{-3} s$, and it takes 1.3×10^7 time steps to obtain the steady results ($u_0 t/H \approx 60$). Fig. 4(b) shows the local Mach number $Ma_l = \frac{\sqrt{u^2 + v^2}}{\sqrt{\gamma RT}}$ contour after the flow reaches a steady state. The local Mach number for this case is very small, the maximum value is around 0.0126. Therefore, while the local Mach number is always small, the compressible effect as seen from the density change is significant due to large temperature changes. The fluid density near the left vertical wall is significantly less than that near the right wall.

The flow at $Ra = 1.0 \times 10^6$ and $\epsilon = 0.6$ can reach a steady state at long times. Fig. 5 shows the isotherms and velocity vector plot. We can clearly observe that the fluid near the hot wall is expanded, and the fluid near the cold wall is contracted. Unlike the Boussinesq flow, the compressible natural convection is no longer symmetric about the cavity center.

Table 5Parameters for the simulation of natural convection with a large temperature difference.

Ra	Pr	γ	ϵ	Ма	$p_0 (\mathrm{kg/m} \mathrm{s}^2)$	T_0 (K)	$R (m^2/s^2 K)$	$g \ (m/s^2)$	μ_0
1.0×10^{6}	0.71	1.4	0.6	4.11×10^{-2}	101325.0	600.0	287	g(Ra)	0.01

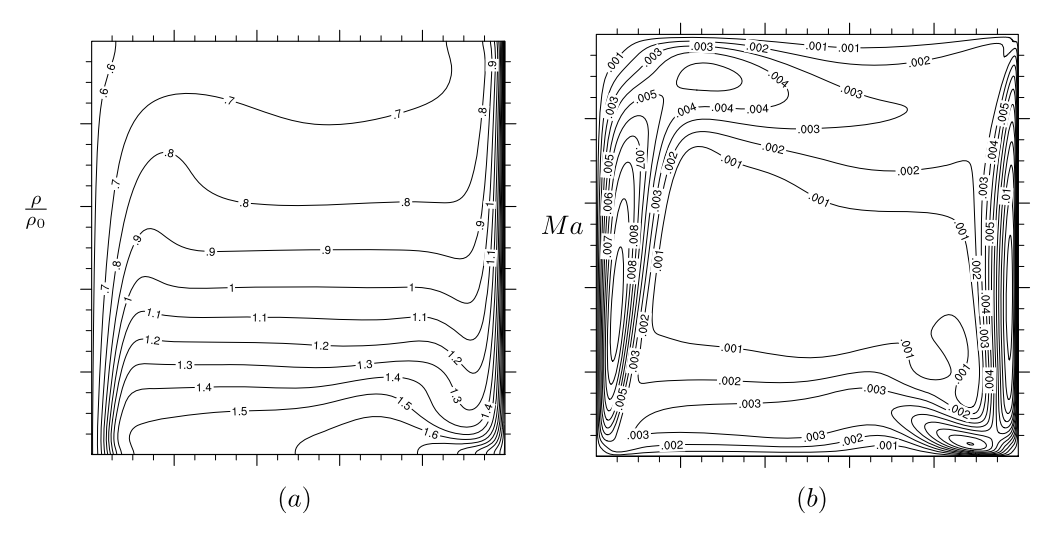


Fig. 4. (a). Density contour; (b), local Mach number contour for compressible natural convection with $Ra = 1.0 \times 10^6$, $\epsilon = 0.6$.

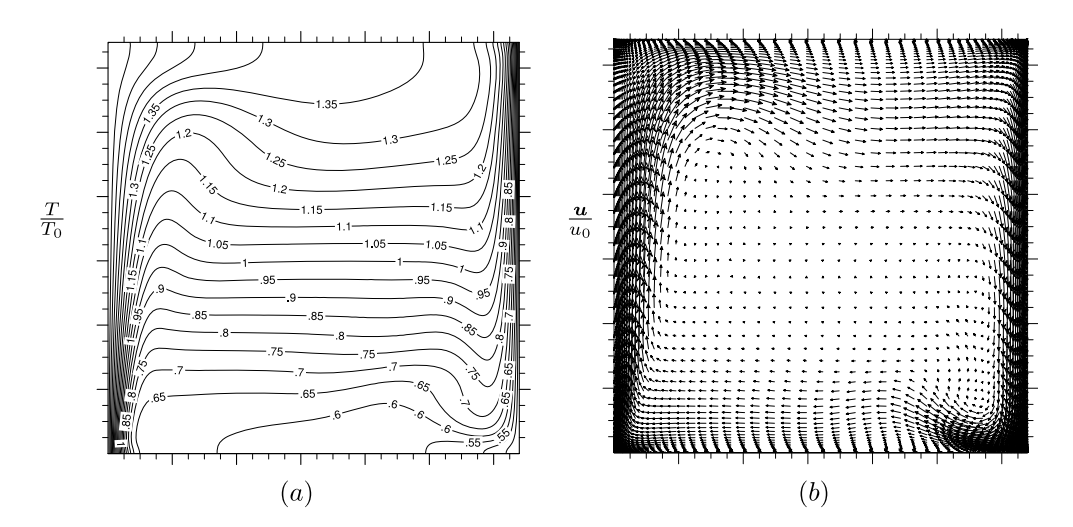


Fig. 5. (a). Isotherms; (b). Velocity vector plot for compressible natural convection with $Ra = 1.0 \times 10^6$, $\epsilon = 0.6$.

Although the temperature is still stratified in the cavity center, the stratification slope is not constant along the vertical direction. As the hot fluid is expanded, it occupies more than half of the cavity domain.

Fig. 6 shows the temperature profiles and velocity profiles at the mid-height and mid-width of the cavity (Pr is added as in the literature $u_0\sqrt{Pr}$ is used as the reference velocity scale). We compare our results with the benchmark results of Vierendeels et al. [15]. Both temperature and velocity profiles are in excellent agreement with the reference solutions. From Fig. 6(a) and (c), we can clearly observe that the boundary layer thickness near the hot wall is large than that near the cold wall. It is natural to expect that for unsteady natural convection simulation at even higher Rayleigh number, the cold wall boundary layer will be extremely thin and requires finer resolution. Again, due to the expansion of the hot fluid, the temperature at the mid-height ($T_{mid} \approx 622$ K) is no longer the same as T_0 , it slightly higher than T_0 (600 K).

Besides the velocity and temperature profiles, we also provide the local Nusselt number distribution along the hot and cold walls. The Nusselt number is calculated as:

$$Nu(x) = \frac{H}{k_0 (T_h - T_c)} k \frac{\partial T}{\partial y} \bigg|_{wall} = -\frac{H}{k_0 (T_h - T_c)} q_y, \tag{28}$$

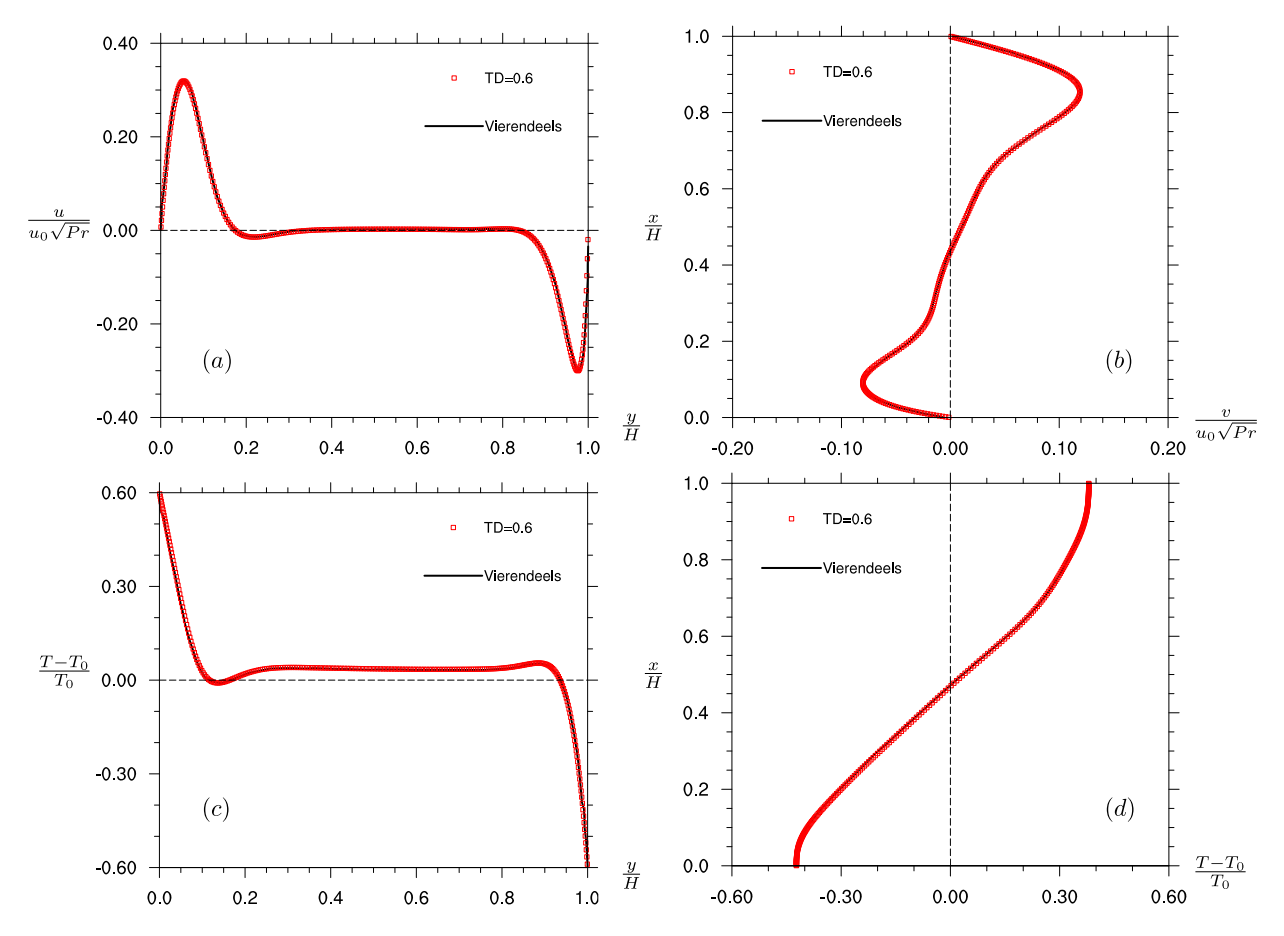


Fig. 6. (a). Vertical velocity u/u_0 and (c). Temperature distribution at the mid-height x = 0.5H; (b). Horizontal velocity v/u_0 and (d). Temperature distribution at the mid-width y = 0.5H for $Ra = 1.0 \times 10^6$, $\epsilon = 0.6$.

where q_y can be computed using the distribution function as $q_y = \frac{1}{2} \int c_y (c^2 g + h) d\xi$. Fig. 7 shows the Nusselt number profiles from Darbandi et al. [48] using a Finite-Volume approach, and those from Heuveline [49] using a Finite-Element method, and current DUGKS simulation. Our results agree well with the solution of Darbandi et al. with 300×300 uniform meshes. Different from the symmetric Nusselt number distribution of the Boussinesq flow, for compressible natural convection the Nusselt number distribution along the hot and cold wall show different distributions. The averaged Nusselt number for two isothermal walls are $\overline{Nu}_h = 8.6874$ and $\overline{Nu}_c = 8.6767$.

3.3. Compressible unsteady natural convection

As the Rayleigh number exceeds a critical value, the flow becomes unsteady, this is the case for fire safety simulations [50]. In this study, we also investigate the unsteady natural convection with $Ra = 5.0 \times 10^9$ and $\epsilon = 0.6$. While for steady compressible natural convection there are several studies available in the literature and the flow features are clear, for unsteady compressible natural convection, the flow statistics and the instability of the boundary layer are not completely clear. To the authors' knowledge, there is only one numerical result reported recently by Lenz et al. [21] using the gas kinetic scheme (GKS) [41]. With the high Rayleigh numbers and a large temperature difference, the flow is unsteady and the flow near the isothermal boundary becomes turbulent. Table 6 shows the parameters for the simulation of unsteady natural convection. We employ the same dimensionless parameters setting as in Lenz et al. [21] The grid resolution used is 360×360 , and the minimal grid spacing near the wall is $\Delta x_{min} = 4.11 \times 10^{-4} H$.

Fig. 8 shows the instantaneous temperature field and time-averaged temperature field. The flow field is averaged over approximately 75 eddy turnover times after the flow reaches statistical stationarity. The eddy turnover time is defined as $\frac{4H}{u_0/3}$, where $u_0/3$ approximates the maximum flow velocity and 4H is the maximum flow path. Interesting flow features can be observed from these temperature contours: the instantaneous temperature contour shows that vortices are generated along the isothermal walls which disturb the flow in the hot wall boundary layer; the flow near the cold wall is more quiescent, vortices are only observed near the bottom corner of the cold wall. These observations are consistent with those reported in Lenz et al., showing that the heating decreases the stability and the cooling increases the stability.

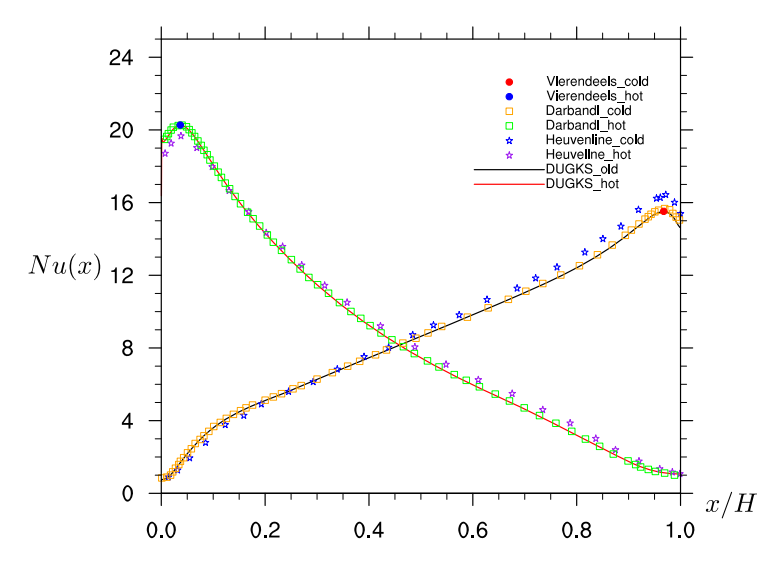


Fig. 7. Nusselt number distribution along the hot and cold walls.

Table 6Parameters for the simulation of compressible unsteady natural convection.

Ra	Pr	γ	ϵ	Ма	$p_0 (kg/m s^2)$	T ₀ (K)	$R (m^2/s^2 K)$	$g (m/s^2)$	μ_0
5.0×10^{9}	0.71	1.4	0.01	0.2927	101325.0	600.0	287	g(Ma)	$\mu(Ra)$

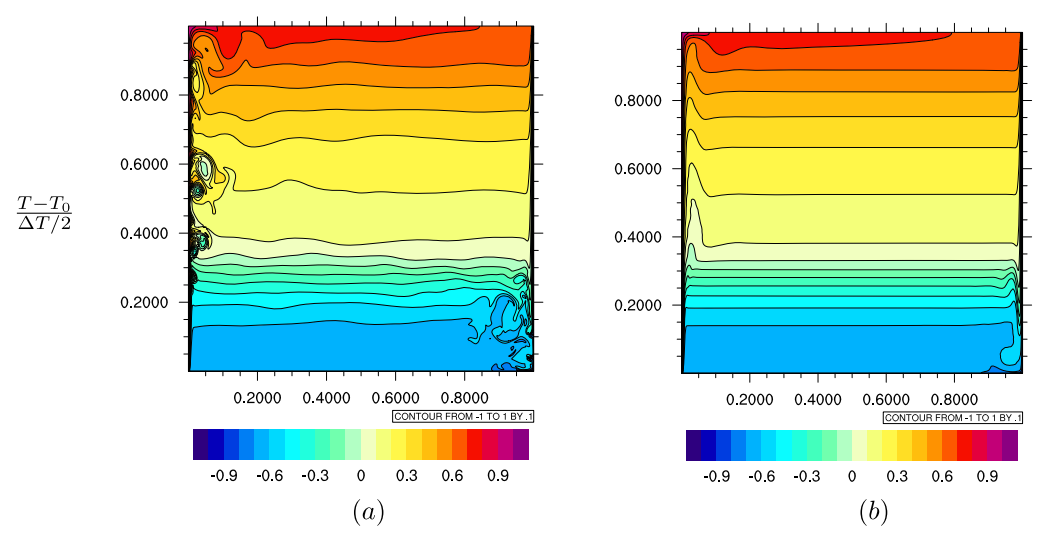


Fig. 8. (a). Instantaneous temperature field; (b). Time-averaged temperature field for natural convection with $Ra = 5.0 \times 10^9$, $\epsilon = 0.6$.

Next, we provide the temperature and velocity profiles at the mid-height and mid-width of the cavity in Fig. 9. Our DUGKS results are in excellent agreement with GKS results of Lenz et al., both methods predict similar velocity and temperature distributions. The profiles show that the velocity and the temperature boundary layer is extremely thin along the cold wall as expected, there are more than 20 cells insides the cold velocity/thermal boundary layer to resolve the steep velocity and temperature gradient. Comparing to vertical velocity profile, the horizontal velocity profile Fig. 9(b) shows relatively complex distributions, the velocity distribution is no longer symmetric about the mid-height and locations corresponding to the peak velocities are intriguing, the maximum horizontal velocity reaches its peak near the upper wall for the hot fluid region, while the maximum velocity of the cold fluid region is near the cavity center. The temperature stratification is altered by the thermal expansion of the fluid, the hot fluid occupies more than $\frac{3}{5}$ region of the cavity, the temperature stratification slopes for the hot fluid region and the cold fluid region are also different. The mean temperature is slightly increased to $\overline{T} \approx 1.045T_0$ in the initial flow developing stage and becomes steady after the flow reaches statistical stationarity.

Turbulent kinetic energy $TKE = \frac{1}{2}(\overline{u'u'} + \overline{v'v'})$ are also computed. For unsteady Boussinesq natural convection, the boundary layer along the isothermal wall experiences laminar, periodic, and eventually a turbulent flow state at the down-

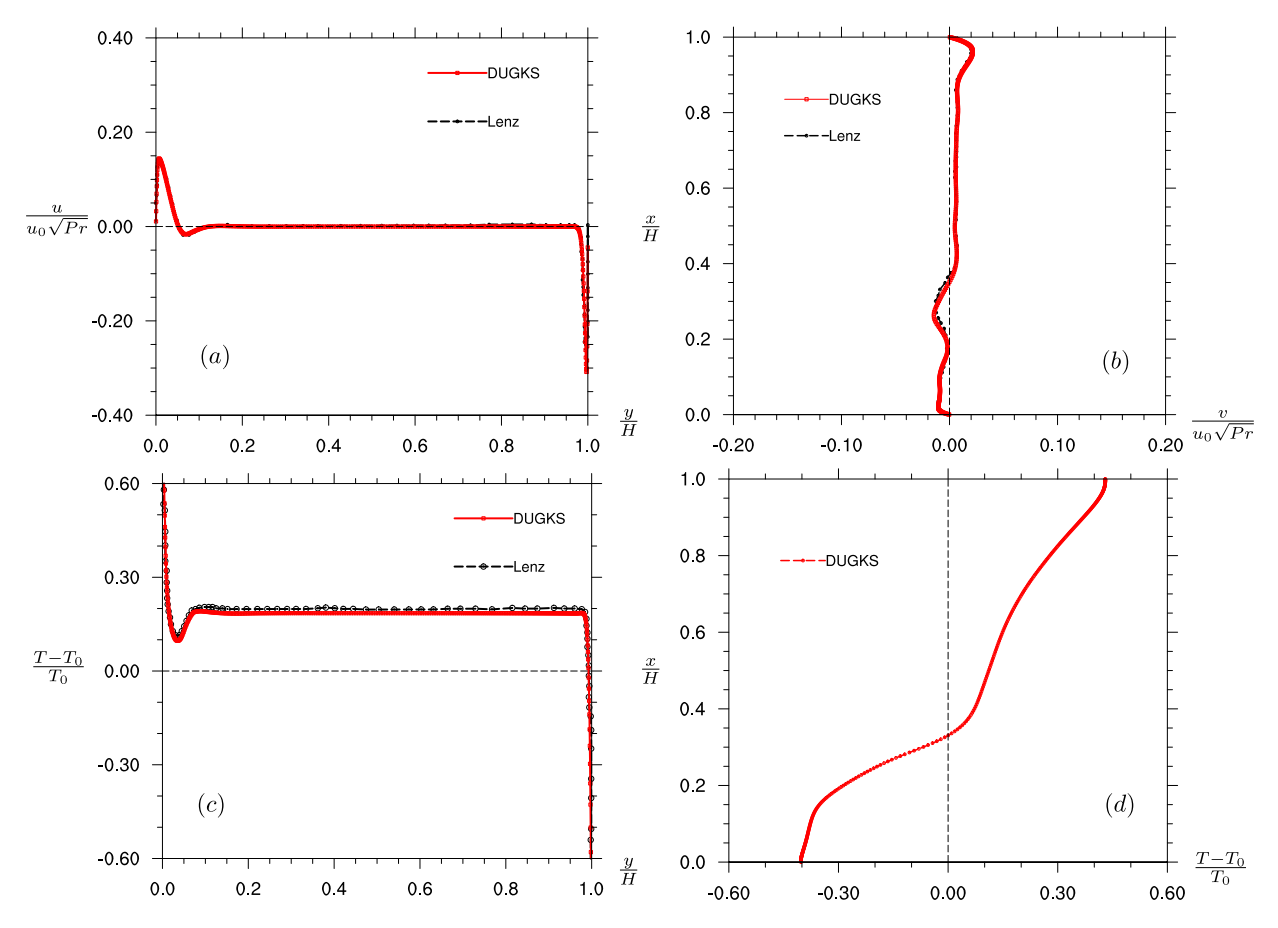


Fig. 9. (a). Vertical velocity and (c). Temperature distribution at the mid-height x = 0.5H; (b). Horizontal velocity and (d). Temperature distribution at the mid-width y = 0.5H for $Ra = 5.0 \times 10^9$, $\epsilon = 0.6$.

stream region of the thermal boundary layer. Trias et al. [51] performed simulations of two-dimensional turbulent natural convection in a tall cavity under the Boussinesq approximation, and for Rayleigh number at $\sim 10^9$ order, all the turbulent fluctuations concentrate at the downstream corner. On the other hand, the unsteady compressible natural convection is characterized by different turbulent flow structures. From Fig. 10, we note that the KTE reaches their maximum near the height x=0.4H for the fluid motion of hot wall. The velocity fluctuations only concentrates at the bottom right corner near the cold wall. This implies that the thermal expansion changes the instability mechanism, the heating of the hot wall destabilizing the hot fluid, while the transition location between steady to unsteady flow moves upstream. The flow structures of the compressible natural convection are highly asymmetric.

4. Conclusion

In this study, we investigate the compressible natural convection using a modified discrete unified gas-kinetic scheme (DUGKS). A source term is introduced to adjust the Prandtl number without increasing the requirement of Gauss-Quadrature quadrature order. A systematic approach of deriving the "bounce-back" boundary condition for the distribution function is suggested, based on the Chapman-Enskog approximation. The current boundary treatment is fully consistent with the compressible Navier-Stokes and energy equations. We show that our scheme can reproduce the Boussinesq results accurately, and is able to simulate fully compressible convection flows.

Two compressible natural convection simulations are performed, steady compressible natural convection at $Ra = 1.0 \times 10^6$ and $\epsilon = 0.6$, and the unsteady natural convection with $Ra = 5.0 \times 10^9$ and $\epsilon = 0.6$. For the former case, we compared the velocity, temperature, and Nusselt number distribution with results from the literature, and show that the solution of our scheme is accurate. And the current scheme is capable of simulating unsteady compressible natural convection, our results agree well with the GKS results of Lenz et al. [21]. Interesting turbulent fluctuation statistics are observed along the hot wall and at the right bottom corner of the cold wall.

In summary, we validate that the discrete unified gas-kinetic scheme is a robust and accurate tool for compressible flow simulations. We develop a modified model which solves the unit Prandtl number limitation of the standard BGK model and provide a systematic approach of deriving better boundary condition treatment. In general, compressible convection flows

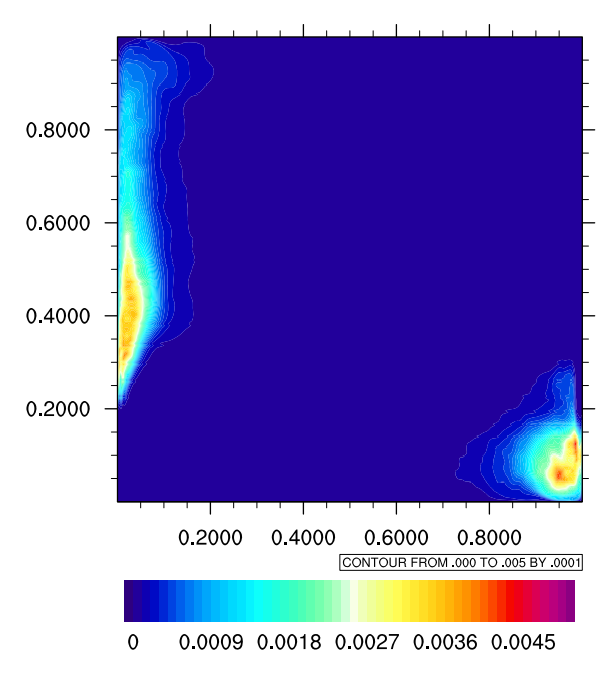


Fig. 10. Turbulent kinetic energy $KTE/(u_0^2Pr)$.

at high Rayleigh numbers are more complex than the Boussinesq convection flows. Kinetic methods such as DUGKS would be a reliable approach for studying the dynamics of compressible convection in the future.

CRediT authorship contribution statement

Xin Wen: Conceptualization, Data curation, Formal analysis, Investigation, Methodology, Project administration, Validation, Writing – original draft, Writing – review & editing. **Lian-Ping Wang:** Conceptualization, Funding acquisition, Investigation, Methodology, Project administration, Resources, Supervision, Writing – review & editing. **Zhaoli Guo:** Conceptualization, Writing – review & editing. **Jie Shen:** Formal analysis, Methodology.

Declaration of competing interest

The authors declare that they have no known competing financial interests or personal relationships that could have appeared to influence the work reported in this paper.

Acknowledgements

This work has been supported by the U.S. National Science Foundation (CNS-1513031, CBET-1706130), the National Natural Science Foundation of China (91852205, 91741101, 12041601 & 11961131006), NSFC Basic Science Center Program (Award number 11988102), the National Numerical Wind Tunnel program, Guangdong Provincial Key Laboratory of Turbulence Research and Applications (2019B21203001), Guangdong-Hong Kong-Macao Joint Laboratory for Data-Driven Fluid Mechanics and Engineering Applications (2020B1212030001), and Shenzhen Science & Technology Program- Grant No. KQTD20180411143441009). Computing resources are provided by the Center for Computational Science and Engineering of Southern University of Science and Technology and by National Center for Atmospheric Research (CISL-UDEL0001).

Appendix A. Hermite expansion of equilibrium

Based on the Chapman-Enskog analysis, the fourth-order moment of the $g^{eq}(\boldsymbol{\xi}, \boldsymbol{x}, t)$ and second-order moment of $h^{eq}(\boldsymbol{\xi}, \boldsymbol{x}, t)$ are needed to obtain the correct heat flux expression in compressible flows. The fourth-order Hermite expansion of $g^{eq,N=4}(\boldsymbol{\xi}, \boldsymbol{x}, t)$ and second-order Hermite expansion of $h^{eq,N=2}(\boldsymbol{\xi}, \boldsymbol{x}, t)$ can be derived and the results are

$$g^{eq,(4)} = \omega \rho \left\{ \begin{aligned} &1 + \frac{\xi_{j} u_{j}}{RT_{0}} + \frac{1}{2} \left[\frac{\left(\xi_{j} u_{j}\right)^{2}}{\left(RT_{0}\right)^{2}} - \frac{u^{2}}{RT_{0}} + (\theta - 1) \left(\frac{\xi^{2}}{RT_{0}} - D \right) \right] \\ &+ \frac{1}{6} \frac{\xi_{j} u_{j}}{RT_{0}} \left[\frac{\left(\xi_{j} u_{j}\right)^{2}}{\left(RT_{0}\right)^{2}} - 3 \frac{u^{2}}{RT_{0}} + 3 (\theta - 1) \left(\frac{\xi^{2}}{RT_{0}} - D - 2 \right) \right] \\ &+ \frac{1}{24} \frac{\left(\xi_{j} u_{j}\right)^{2}}{\left(RT_{0}\right)^{2}} \left[\frac{\left(\xi_{j} u_{j}\right)^{2}}{\left(RT_{0}\right)^{2}} - 6 \frac{u^{2}}{RT_{0}} + 6 (\theta - 1) \left(\frac{\xi^{2}}{RT_{0}} - D - 4 \right) \right] \\ &+ \frac{1}{8} \frac{u^{2}}{RT_{0}} \left[\frac{u^{2}}{RT_{0}} + 2 (\theta - 1) \left(- \frac{\xi^{2}}{RT_{0}} + D + 2 \right) \right] \\ &+ \frac{1}{8} (\theta - 1)^{2} \left[\frac{\xi^{4}}{\left(RT_{0}\right)^{2}} - (2D + 4) \frac{\xi^{2}}{RT_{0}} + D^{2} + 2D \right] \end{aligned} \right\}$$
(A.1)

$$h^{eq,(2)} = \omega \tilde{K} \rho RT \left\{ 1 + \frac{\xi_j u_j}{RT_0} + \frac{1}{2} \frac{(\xi_j u_j)^2}{(RT_0)^2} - \frac{1}{2} \frac{u^2}{RT_0} \right\} + \mathcal{O}(Ma^3),$$

$$\left\{ + \frac{1}{2} (\theta - 1) \left(\frac{\xi^2}{RT_0} - D \right) \right\}$$
(A.2)

where subscript a represents the index of discrete particle velocities. The following relations can be derived for the use of the boundary condition derivation.

$$g^{eq+} + g^{eq-} = 2W_a \rho \left\{ \begin{aligned} 1 + \frac{1}{2} \left[\frac{\left(\xi_{a,j} u_j\right)^2}{(RT_0)^2} - \frac{u^2}{RT_0} + (\theta - 1) \left(\frac{\xi_a^2}{RT_0} - D \right) \right] \\ + \frac{1}{24} \frac{\left(\xi_{a,j} u_j\right)^2}{(RT_0)^2} \left[\frac{\left(\xi_{a,j} u_j\right)^2}{(RT_0)^2} - 6 \frac{u^2}{RT_0} \\ + 6 \left(\theta - 1\right) \left(\frac{\xi_a^2}{RT_0} - D - 4 \right) \right] \\ + \frac{1}{8} \frac{u^2}{RT_0} \left[\frac{u^2}{RT_0} + 2 \left(\theta - 1\right) \left(- \frac{\xi_a^2}{RT_0} + D + 2 \right) \right] \\ + \frac{1}{8} \left(\theta - 1\right)^2 \left[\frac{\xi_a^4}{(RT_0)^2} - (2D + 4) \frac{\xi_a^2}{RT_0} + D^2 + 2D \right] \end{aligned} \right\}, \tag{A.3a}$$

$$g^{eq+} - g^{eq-} = 2W_a \rho \left\{ \frac{\xi_{a,j} u_j}{RT_0} + \frac{1}{6} \frac{\xi_{a,j} u_j}{RT_0} \begin{bmatrix} \frac{\left(\xi_{a,j} u_j\right)^2}{\left(RT_0\right)^2} - 3\frac{u^2}{RT_0} \\ + 3\left(\theta - 1\right) \left(\frac{\xi_a^2}{RT_0} - D - 2\right) \end{bmatrix} \right\}, \tag{A.3b}$$

$$h^{eq+} + h^{eq-} = 2W_a \tilde{K} \rho RT \left\{ 1 + \frac{1}{2} \left[\frac{\left(\xi_{a,j} u_j \right)^2}{\left(RT_0 \right)^2} - \frac{u^2}{RT_0} + (\theta - 1) \left(\frac{\xi_a^2}{RT_0} - D \right) \right] \right\}, \tag{A.3c}$$

$$h^{eq+} - h^{eq-} = 2W_a \tilde{K} \rho RT \left\{ \frac{\xi_{a,j} u_j}{RT_0} \right\}. \tag{A.3d}$$

where $\xi_{a,j}$ and W_a are the abscissa and the corresponding weights of the chosen quadrature. For simplicity, we use superscript + to represent the particles $\xi_{\bar{a}}$ bounce back from the wall, while the superscript - represents the particles $\xi_{\bar{a}}$ moving towards the wall.

Appendix B. Heat flux and Prandtl number correction

The heat flux q_i can be computed from two reduced distribution functions as:

$$\begin{split} q_{i} &= \frac{1}{2} \int c_{i} \left(c^{2} g + h \right) d\xi \\ &= \frac{1}{2} \int c_{i} c^{2} \left\{ g^{eq} - \tau \left[\frac{\partial g^{eq}}{\partial t} + \xi_{j} \frac{\partial g^{eq}}{\partial x_{j}} + b_{j} \frac{\partial g^{eq}}{\partial \xi_{j}} \right] \right\} d\xi \\ &+ \frac{1}{2} \int c_{i} \left\{ h^{eq} + \tau S_{h} - \tau \left[\frac{\partial h^{eq}}{\partial t} + \xi_{j} \frac{\partial h^{eq}}{\partial x_{j}} + b_{j} \frac{\partial h^{eq}}{\partial \xi_{j}} \right] \right\} d\xi \\ &= -\frac{1}{2} \tau \left\{ \int c_{i} c^{2} \left[\frac{\partial g^{eq}}{\partial t} + \xi_{j} \frac{\partial g^{eq}}{\partial x_{j}} + b_{j} \frac{\partial g^{eq}}{\partial \xi_{j}} \right] d\xi \right\} \\ &+ \int c_{i} \left[\frac{\partial h^{eq}}{\partial t} + \xi_{j} \frac{\partial h^{eq}}{\partial x_{j}} + b_{j} \frac{\partial h^{eq}}{\partial \xi_{j}} \right] d\xi \right\} + \frac{1}{2} \int c_{i} \tau S_{h} d\xi. \end{split}$$
(B.1)

The first part of integration results in a value of $-p\tau C_p \frac{\partial T}{\partial x_i}$, the second part yields $\frac{1}{2} \int c_i \tau S_h d\xi = (1-Pr)q_i$. The actual thermal conductivity becomes $k = \frac{p\tau C_p}{Pr}$, the Prandtl number can be altered through this relatively simple approach without increase the Gauss quadrature requirement of the scheme.

Appendix C. The Chapman Enskog analysis of boundary condition

To derive the boundary condition, we employ the Chapman-Enskog expansion to the order of τ , the distribution function $g(\xi, \mathbf{x}, t)$ and $h(\xi, \mathbf{x}, t)$ can be obtained from Eq. (12) as:

$$g = g^{eq} - \tau \left[\frac{\partial g^{eq}}{\partial t} + \xi_j \frac{\partial g^{eq}}{\partial x_j} + b_j \frac{\partial g^{eq}}{\partial \xi_j} \right] + \mathcal{O}(\tau^2), \tag{C.1a}$$

$$h = h^{eq} + \tau S_h - \tau \left[\frac{\partial h^{eq}}{\partial t} + \xi_j \frac{\partial h^{eq}}{\partial x_j} + b_j \frac{\partial h^{eq}}{\partial \xi_j} \right] + \mathcal{O}(\tau^2). \tag{C.1b}$$

The derivatives $\frac{\partial g^{eq}}{\partial t}$, $\frac{\partial g^{eq}}{\partial x_j}$, $\frac{\partial g^{eq}}{\partial \xi_j}$, $\frac{\partial h^{eq}}{\partial t}$, $\frac{\partial h^{eq}}{\partial t}$, $\frac{\partial h^{eq}}{\partial \xi_j}$ can be evaluated directly using the expression of equilibriums Eq. (13).

$$\frac{\partial g^{eq}}{\partial t} = g^{eq} \left\{ \frac{\partial \ln \rho}{\partial t} + \left(\frac{c^2}{2RT} - \frac{D}{2} \right) \frac{\partial \ln T}{\partial t} + \frac{c_k}{RT} \frac{\partial u_k}{\partial t} \right\},\tag{C.2a}$$

$$\frac{\partial g^{eq}}{\partial x_i} = g^{eq} \left\{ \frac{\partial \ln \rho}{\partial x_i} + \left(\frac{c^2}{2RT} - \frac{D}{2} \right) \frac{\partial \ln T}{\partial x_i} + \frac{c_k}{RT} \frac{\partial u_k}{\partial x_i} \right\},\tag{C.2b}$$

$$\frac{\partial g^{eq}}{\partial \xi_j} = -\frac{c_j}{RT} g^{eq},\tag{C.2c}$$

$$\frac{\partial h^{eq}}{\partial t} = \tilde{K}RTg^{eq} \left\{ \frac{1}{T} \frac{\partial T}{\partial t} + \left[\frac{\partial \ln \rho}{\partial t} + \left(\frac{c^2}{2RT} - \frac{D}{2} \right) \frac{\partial \ln T}{\partial t} + \frac{c_k}{RT} \frac{\partial u_k}{\partial t} \right] \right\}, \tag{C.3a}$$

$$\frac{\partial h^{eq}}{\partial x_i} = \tilde{K}RTg^{eq} \left\{ \frac{1}{T} \frac{\partial T}{\partial x_i} + \left[\frac{\partial \ln \rho}{\partial x_i} + \left(\frac{c^2}{2RT} - \frac{D}{2} \right) \frac{\partial \ln T}{\partial x_i} + \frac{c_k}{RT} \frac{\partial u_k}{\partial x_i} \right] \right\},\tag{C.3b}$$

$$\frac{\partial h^{eq}}{\partial \xi_j} = -\frac{c_j}{RT} h^{eq}. \tag{C.3c}$$

To remove all the time derivatives, the leading-order Euler equations are used here:

$$\frac{\partial \rho}{\partial t} = -\frac{\partial \rho u_j}{\partial x_j} + \mathcal{O}(\tau),\tag{C.4a}$$

$$\rho \frac{\partial u_i}{\partial t} = -\rho u_j \frac{\partial u_i}{\partial x_j} - \frac{\partial \rho RT}{\partial x_i} + \rho b_i + \mathcal{O}(\tau), \tag{C.4b}$$

$$\rho C_V \frac{\partial T}{\partial t} = -\rho C_V u_J \frac{\partial T}{\partial x_J} - p \frac{\partial u_k}{\partial x_k} + \mathcal{O}(\tau). \tag{C.4c}$$

Then we can obtain the structure of the distribution functions of g and h as:

$$g = g^{eq} \left\{ 1 - \frac{\tau c_i c_j}{RT} \frac{\partial u_i}{\partial x_j} + \tau \left[\frac{c^2}{(K+3)RT} + \frac{\tilde{K}}{K+3} \right] \frac{\partial u_j}{\partial x_j} \right\} + \mathcal{O}(\tau^2),$$

$$\left\{ -\tau c_j \frac{\partial T}{\partial x_j} \left(\frac{c^2}{2RT^2} - \frac{D+2}{2T} \right) \right\}$$
(C.5a)

$$h = h^{eq} \begin{cases} 1 - \frac{\tau c_i c_j}{RT} \frac{\partial u_i}{\partial x_j} + \tau \left[\frac{c^2}{(K+3)RT} + \frac{\tilde{K}+2}{K+3} \right] \frac{\partial u_j}{\partial x_j} \\ - \tau c_j \frac{\partial T}{\partial x_j} \left(\frac{c^2}{2RT^2} - \frac{D}{2T} \right) \end{cases} + \tau S_h + \mathcal{O}(\tau^2).$$
(C.5b)

The above distributions are fully consistent with the Chapman-Enskog expansion. The non-equilibrium part of distribution function contains contributions associated with the strain rate and heat flux. Based on the above results, we can derive the kinetic treatment of the boundary conditions.

First, for no-slip velocity boundary condition we can write:

$$g(\xi_{a,j}) - g(\xi_{\bar{a},j}) = \begin{cases} 1 - \frac{\tau(\xi_{a,i}\xi_{a,j} + u_{i}u_{j})}{RT} \frac{\partial u_{i}}{\partial x_{j}} + \tau \left[\frac{\xi_{a}^{2} + u^{2}}{(K+3)RT} + \frac{\tilde{K}}{K+3} \right] \frac{\partial u_{j}}{\partial x_{j}} \\ + \tau \frac{\partial T}{\partial x_{j}} \left[\frac{\xi_{a}^{2}u_{j} + 2\xi_{a,i}\xi_{a,j}u_{i} + u_{j}u^{2}}{2RT^{2}} - \frac{u_{j}(D+2)}{2T} \right] \end{cases}$$

$$+ (g^{eq+} + g^{eq-}) \begin{cases} \frac{\tau(\xi_{a,i}u_{j} + \xi_{a,j}u_{i})}{RT} \frac{\partial u_{i}}{\partial x_{j}} - \frac{\tau 2\xi_{a,i}u_{i}}{(K+3)RT} \frac{\partial u_{j}}{\partial x_{j}} \\ - \tau \frac{\partial T}{\partial x_{j}} \left[\frac{\xi_{a}^{2}\xi_{a,j} + 2\xi_{a,i}u_{i}u_{j} + \xi_{a,j}u^{2}}{2RT^{2}} - \frac{\xi_{a,j}(D+2)}{2T} \right] \end{cases}$$

$$+ \mathcal{O}(\tau^{2}).$$
(C.6)

With the condition $\boldsymbol{u}_w = 0$, the equation above can be simplified to:

$$g(\xi_{a,j}) - g(\xi_{\bar{a},j}) = (g^{eq+} - g^{eq-}) \left\{ 1 - \frac{\tau(\xi_{a,i}\xi_{a,j})}{RT} \frac{\partial u_i}{\partial x_j} + \tau \left[\frac{\xi_a^2}{(K+3)RT} + \frac{\tilde{K}}{K+3} \right] \frac{\partial u_j}{\partial x_j} \right\}$$

$$+ (g^{eq+} + g^{eq-}) \left\{ - \tau \frac{\partial T}{\partial x_j} \left[\frac{\xi_a^2 \xi_{a,j}}{2RT^2} - \frac{\xi_{a,j}(D+2)}{2T} \right] \right\} + \mathcal{O}(\tau^2)$$
(C.7)

Substituting the relations Eq. (A.3) into the equation above, the term $(g^{eq+} - g^{eq-})$ equals zero with the condition $\mathbf{u}_w = 0$. Then the equation becomes:

$$g(\xi_{a,j}) - g(\xi_{\bar{a},j}) = 2W_{a}\rho \left\{ 1 + \frac{1}{2} \left[(\theta - 1) \left(\frac{\xi_{a}^{2}}{RT_{0}} - D \right) \right] + \frac{1}{8} (\theta - 1)^{2} \left[\frac{\xi_{a}^{4}}{(RT_{0})^{2}} - (2D + 4) \frac{\xi_{a}^{2}}{RT_{0}} + D^{2} + 2D \right] \right\}$$

$$\times \left\{ -\tau \frac{\partial T}{\partial x_{j}} \left[\frac{\xi_{a}^{2} \xi_{a,j}}{2RT^{2}} - \frac{\xi_{a,j} (D + 2)}{2T} \right] \right\} + \mathcal{O}(\tau^{2}).$$
(C.8)

Besides, to be consistent with the Hermite expansion of equilibrium, we expand 1/T to the order of Ma^4 :

$$\frac{1}{T} = \frac{1}{T_0} \frac{1}{1 + \frac{T - T_0}{T_0}} \approx \frac{1}{T_0} \left[1 - (\theta - 1) + (\theta - 1)^2 \right] + \mathcal{O}(Ma^5), \tag{C.9a}$$

$$\frac{1}{T^2} \approx \frac{1}{T_0^2} \left[1 - 2(\theta - 1) + 3(\theta - 1)^2 \right] + \mathcal{O}(Ma^5). \tag{C.9b}$$

Submitting the expanded temperature terms into the Eq. (C.8), we have:

$$g(\xi_{a,j}) - g(\xi_{\bar{a},j}) = 2W_{a}\rho \left\{ 1 + \frac{1}{2} \left[(\theta - 1) \left(\frac{\xi_{a}^{2}}{RT_{0}} - D \right) \right] + \frac{1}{8} (\theta - 1)^{2} \left[\frac{\xi_{a}^{4}}{(RT_{0})^{2}} - (2D + 4) \frac{\xi_{a}^{2}}{RT_{0}} + D^{2} + 2D \right] \right\}$$

$$\times \left\{ -\tau \xi_{j} \frac{\partial T}{\partial x_{j}} \left[\frac{\xi^{2}}{2RT_{0}^{2}} [1 - 2(\theta - 1) + 3(\theta - 1)^{2}] - \frac{(D + 2)}{2T_{0}} [1 - (\theta - 1) + (\theta - 1)^{2}] \right] \right\}.$$
(C.10)

All the terms with order higher than $\mathcal{O}(Ma^5)$ can be neglected. Finally, we can obtain the no-slip boundary as:

$$g(\xi_{a,j}) = g(\xi_{\bar{a},j}) - \tau W_a \rho \frac{\xi_{a,j}}{T_0} \frac{\partial T}{\partial x_j} \begin{cases} \left(\frac{\xi_a^2}{RT_0} - D - 2\right) \\ \frac{1}{2}(\theta - 1) \left[\frac{\xi_a^4}{(RT_0)^2} - 2(D+3)\frac{\xi_a^2}{RT_0} + (D+2)^2\right] \\ \frac{1}{8}(\theta - 1)^2 \left[\frac{\xi_a^6}{(RT_0)^3} - (3D+14)\frac{\xi_a^4}{(RT_0)^2} + (D+4)(3D+10)\frac{\xi_a^2}{(RT_0)} - (D+2)^2(D+4) \right] \end{cases} + \mathcal{O}(\tau^2, Ma^5)$$
(C.11)

For adiabatic thermal boundary condition, we have $u_w = 0$ and $\frac{\partial T}{\partial n} = 0$. From Eq. (C.5b), we can obtain

$$h(\xi_{a,j}) - h(\xi_{\bar{a},j}) = (h^{eq+} - h^{eq-}) \begin{cases} 1 - \frac{\tau(\xi_{a,i}\xi_{a,j} + u_iu_j)}{RT} \frac{\partial u_i}{\partial x_j} \\ + \tau \left[\frac{\xi_a^2 + u^2}{(K+3)RT} + \frac{\tilde{K} + 2}{K+3} \right] \frac{\partial u_j}{\partial x_j} \\ + \tau \frac{\partial T}{\partial x_j} \left[\frac{\xi_a^2 u_j + 2\xi_{a,i}\xi_{a,j}u_i + u_ju^2}{2RT^2} - \frac{u_jD}{2T} \right] \end{cases}$$

$$+ (h^{eq+} + h^{eq-}) \begin{cases} \frac{\tau(\xi_{a,i}u_j + \xi_{a,j}u_i)}{RT} \frac{\partial u_i}{\partial x_j} - \frac{\tau 2\xi_{a,i}u_i}{(K+3)RT} \frac{\partial u_j}{\partial x_j} \\ - \tau \frac{\partial T}{\partial x_j} \left[\frac{\xi_a^2 \xi_{a,j} + 2\xi_{a,i}u_iu_j + \xi_{a,j}u^2}{2RT^2} - \frac{\xi_{a,j}D}{2T} \right] \end{cases}$$

$$+ 2\tau S_{h,a} + \mathcal{O}(\tau^2).$$
(C.12)

Similar process as before, but the 1/T only needs to be expanded to the Ma^2 for the h distribution as:

$$\frac{1}{T} = \frac{1}{T_0} \frac{1}{1 + \frac{T - T_0}{T_0}} \approx \frac{1}{T_0} \left[1 - (\theta - 1) \right] + \mathcal{O}(Ma^3). \tag{C.13}$$

After substituting the equilibrium and neglecting high order terms, the adiabatic boundary condition can be written as:

$$h(\xi_{a,j}) = h(\xi_{\bar{a},j}) - \tilde{K}\rho R\tau W_a \xi_{a,j} \frac{\partial T}{\partial x_j} \left\{ \left(\frac{\xi_a^2}{RT_0} - D \right) + \frac{1}{2} (\theta - 1) \left[\frac{\xi_a^4}{(RT_0)^2} - 2(D+1) \frac{\xi_a^2}{RT_0} + D^2 \right] \right\} + 2W_a \frac{2(1-Pr)}{\sqrt{RT_0}} \frac{\xi_a \cdot \mathbf{q}}{\sqrt{RT_0}} + \mathcal{O}(\tau^2, Ma^3),$$
(C.14)

For the isothermal boundary condition, the wall temperature is fixed $T = T_w$. From Eq. (C.5b) we have:

$$h(\xi_{a,j}) + h(\xi_{\tilde{a},j}) = (h^{eq+} + h^{eq-}) \begin{cases} 1 - \frac{\tau(\xi_{a,i}\xi_{a,j} + u_{i}u_{j})}{RT} \frac{\partial u_{i}}{\partial x_{j}} \\ + \tau \left[\frac{\xi_{a}^{2} + u^{2}}{(K+3)RT} + \frac{\tilde{K} + 2}{K+3} \right] \frac{\partial u_{j}}{\partial x_{a,j}} \\ + \tau \frac{\partial T}{\partial x_{j}} \left[\frac{\xi_{a}^{2}u_{j} + 2\xi_{a,i}\xi_{a,j}u_{i} + u_{j}u^{2}}{2RT^{2}} - \frac{u_{j}D}{2T} \right] \end{cases}$$

$$+ (h^{eq+} - h^{eq-}) \begin{cases} \frac{\tau(\xi_{a,i}u_{j} + \xi_{a,j}u_{i})}{RT} \frac{\partial u_{i}}{\partial x_{j}} - \frac{\tau 2\xi_{a,i}u_{i}}{(K+3)RT} \frac{\partial u_{j}}{\partial x_{j}} \\ - \tau \frac{\partial T}{\partial x_{j}} \left[\frac{\xi_{a}^{2}\xi_{a,j} + 2\xi_{a,i}u_{i}u_{j} + \xi_{a,j}u^{2}}{2RT^{2}} - \frac{\xi_{a,j}D}{2T} \right] \end{cases}$$

$$+ 2\tau S_{h,a} + \mathcal{O}(\tau^{2}).$$
(C.15)

Substituting the equilibrium and apply the condition $\mathbf{u}_{w} = 0$, we can get:

$$h(\xi_{a,j}) + h(\xi_{\bar{a},j}) = 2W_a (K+3-D) \rho RT \left[1 + \frac{1}{2} \left(\frac{T}{T_0} - 1 \right) \left(\frac{\xi_a^2}{RT_0} - D \right) \right]$$

$$\times \left\{ 1 - \frac{\tau \xi_{a,i} \xi_{a,j}}{RT} \frac{\partial u_i}{\partial x_j} + \tau \left[\frac{\xi_a^2}{(K+3)RT} + \frac{K+5-D}{K+3} \right] \frac{\partial u_j}{\partial x_j} \right\} + \mathcal{O}(\tau^2),$$
(C.16)

where 1/T needs to be expanded to Ma^2 , and finally we can obtain the isothermal boundary condition as:

$$h(\xi_{a,j}) = -h(\xi_{\tilde{a},j}) + 2W_{a}\tilde{K}p \left[1 + \frac{1}{2} (\theta - 1) \left(\frac{\xi_{a}^{2}}{RT_{0}} - D \right) \right]$$

$$+ 2\tau W_{a}\tilde{K}p \frac{\partial u_{j}}{\partial x_{j}} \left[(2 - \theta) \frac{\xi_{a}^{2}}{(K+3)RT_{0}} + \frac{\tilde{K}+2}{K+3} + \frac{1}{2} (\theta - 1) \left(\frac{\xi_{a}^{2}}{RT_{0}} - D \right) \left(\frac{\xi_{a}^{2}}{(K+3)RT_{0}} + \frac{\tilde{K}+2}{K+3} \right) \right]$$

$$+ 2\tau W_{a}\tilde{K}p \frac{\xi_{a,i}\xi_{a,j}}{RT_{0}} \frac{\partial u_{i}}{\partial x_{j}} \left[\theta - 2 - \frac{1}{2} (\theta - 1) \left(\frac{\xi_{a}^{2}}{RT_{0}} - D \right) \right] + \mathcal{O}(\tau^{2}, Ma^{3}).$$
(C.17)

It is important to point out that we did not make any assumption in the derivation. Therefore, these boundary treatments are valid for all compressible continuum flows.

References

- [1] P.I. Bhatnagar, E.P. Gross, M. Krook, A model for collision process in gases. I. Small amplitude processes in charged and neutral one-component systems, Phys. Rev. 94 (1954) 511–525.
- [2] T. Fusegi, J.M. Hyun, Laminar and transitional natural convection in an enclosure with complex and realistic conditions, Int. J. Heat Fluid Flow 15 (4) (1994) 158–168.
- [3] J.R. Lee, On the three-dimensional effect for natural convection in horizontal enclosure with an adiabatic body: review from 2D results and visualization of 3D flow structure, Int. Commun. Heat Mass Transf. 92 (2018) 31–38.
- [4] S. Pandey, Y.G. Park, M.Y. Ha, An exhaustive review of studies on natural convection in enclosures with and without internal bodies of various shapes, Int. J. Heat Mass Transf. 138 (2019) 762–795.
- [5] S. Ostrach, Natural convection in enclosures, Adv. Heat Transf. 8 (1972) 161-227.
- [6] G. de Vahl Davis, G.D. Mallinson, Three-dimensional natural convection in a box: a numerical study, J. Fluid Mech. 93 (1977) 1-31.
- [7] P.L. Quéré, Accurate solutions to the square thermally driven cavity at high Rayleigh number, Comput. Fluids 20 (1991) 29-41.
- [8] P.L. Quéré, M. Behnia, From onset of unsteadiness to chaos in a differentially heated square cavity, J. Fluid Mech. 359 (1998) 81-107.
- [9] S. Paolucci, D.R. Chenoweth, Transition to chaos in a differentially heated vertical cavity, J. Fluid Mech. 201 (1989) 379-410.
- [10] X. Wen, L.P. Wang, Z.L. Guo, D.B. Zhakebayev, Laminar to turbulent flow transition inside the boundary layer adjacent to isothermal wall of natural convection flow in a cubical cavity, Int. J. Heat Mass Transf. 167 (2021) 120822.
- [11] D.R. Chenoweth, S. Paolucci, Natural convection in an enclosed vertical air layer with large horizontal temperature differences, J. Fluid Mech. 169 (1986) 173–210.
- [12] S. Paolucci, On the filtering of sound from the Navier-Stokes equations, Sandia National Laboratories Rep. SAND82-8257, 1982, pp. 1-54.
- [13] P.L. Quéré, R. Masson, P. Perrot, A Chebyshev collocation algorithm for 2D non-Boussinesq convection, J. Comput. Phys. 103 (1992) 302-335.
- [14] J. Vierendeels, B. Merci, E. Dick, Numerical study of natural convective heat transfer with large temperature differences, Int. J. Numer. Methods Heat Fluid Flow 11 (2001) 329–341.
- [15] J. Vierendeels, B. Merci, E. Dick, Benchmark solutions for the natural convective heat transfer problem in a square cavity with large horizontal temperature differences, Int. J. Numer. Methods Heat Fluid Flow 13 (2003) 1057–1078.

- [16] K. Xu, S.H. Lui, Rayleigh-Bénard simulation using the gas-kinetic Bhatnagar-Gross-Krook scheme in the incompressible limit, Phys. Rev. E 60 (1) (1999) 464–470.
- [17] J. Wang, D. Wang, P. Lallemand, L.S. Luo, Lattice Boltzmann simulation of thermal convective flow in two dimensions, Comput. Math. Appl. 65 (2013) 262–286.
- [18] P. Wang, S. Tao, Z.L. Guo, A coupled discrete unified gas-kinetic scheme for Boussinesq flows, Comput. Fluids 120 (2015) 70-81.
- [19] Q. Li, K.H. Luo, Y.L. He, W.Q. Tao, Coupling lattice Boltzmann model for simulation of thermal flows on standard lattices, Phys. Rev. E 85 (2012) 016710.
- [20] Y.L. Feng, P. Sagaut, W.Q. Tao, A three dimensional lattice model for thermal compressible flow on standard lattices, J. Comput. Phys. 303 (2015) 514–529
- [21] S. Lenz, M. Krafczyk, M. Geier, S.Z. Chen, Z.L. Guo, Validation of a two-dimensional gas-kinetic scheme for compressible natural convection on structured and unstructured meshes, Int. J. Therm. Sci. 136 (2019) 299–315.
- [22] F.J. Alexander, H. Chen, S. Chen, G.D. Doolen, Lattice Boltzmann model for compressible fluids, Phys. Rev. A 46 (1992) 1967-1970.
- [23] X.Y. He, S.Y. Chen, G.D. Doolen, A novel thermal model for the lattice Boltzmann method in incompressible limit, J. Comput. Phys. 146 (1998) 282–300.
- [24] P. Lallemand, L.S. Luo, Hybrid finite-difference thermal lattice Boltzmann equation, Int. J. Mod. Phys. B 17 (2003) 41-47.
- [25] Z.L. Guo, C. Zheng, B.C. Shi, T.S. Zhao, Thermal lattice Boltzmann equation for low Mach number flows: decoupling model, Phys. Rev. E 75 (2007) 036704.
- [26] P.L. Quéré, C. Weisman, H. Paillére, J. Vierendeels, E. Dick, R. Becker, M. Braack, J. Jocke, Modeling of natural convection flows with large temperature differences: a benchmark problem for low Mach number solvers. part 1. reference solutions, ESAIM: Math. Model. Numer. Anal. 39 (2005) 609–616.
- [27] H. Paillére, P.L. Quéré, C. Weisman, J. Vierendeels, E. Dick, M. Braack, F. Dabbene, A. Beccantini, E. Studer, T. Kloczko, C. Corre, V. Heuveline, M. Darbandi, S.F. Hosseinizadeh, Modeling of natural convection flows with large temperature differences: a benchmark problem for low Mach number solvers. Part 2. Contribution to the June 2004 conference, ESAIM: Math. Model. Numer. Anal. 39 (2005) 617–621.
- [28] R. Becker, M. Braack, Solution of a stationary benchmark problem for natural convection with large temperature difference, Int. J. Therm. Sci. 41 (2002) 428–439.
- [29] Y.L. Feng, S.L. Guo, W.Q. Tao, P. Sagaut, Regularized thermal lattice Boltzmann method for natural convection with large temperature differences, Int. J. Heat Mass Transf. 125 (2018) 1379–1391.
- [30] Z.L. Guo, R.J. Wang, K. Xu, Discrete unified gas kinetic scheme for all Knudsen number flow: low-speed isothermal case, Phys. Rev. E 88 (2013) 033305.
- [31] Z.L. Guo, R.J. Wang, K. Xu, Discrete unified gas kinetic scheme for all Knudsen number flow. Thermal compressible case, Phys. Rev. E 91 (2015) 1033313.
- [32] Z.L. Guo, K. Xu, Discrete unified gas kinetic scheme for multiscale heat transfer based on the phonon Boltzmann transport equation, Int. J. Heat Mass Transf. 102 (2016) 944–958.
- [33] P. Wang, L.H. Zhu, Z.L. Guo, K. Xu, A comparative study of LBE and DUGKS methods for nearly incompressible flows, Int. J. Heat Mass Transf. 102 (2016) 944–958.
- [34] T. Chen, X. Wen, L.P. Wang, Z.L. Guo, J.C. Wang, S.Y. Chen, Simulation of three-dimensional compressible decaying isotropic turbulence using a redesigned discrete unified gas kinetic scheme, Phys. Fluids 32 (2020) 125104.
- [35] T. Chen, X. Wen, L.P. Wang, Z.L. Guo, J.C. Wang, S.Y. Chen, D.B. Zhakebayev, Simulation of three-dimensional forced compressible isotropic turbulence by a redesigned discrete unified gas kinetic scheme, J. Comput. Phys. (2021) (under revision).
- [36] C. Li, L.P. Wang, An immersed boundary-discrete unified gas kinetic scheme for simulating natural convection involving curved surface, Int. J. Heat Mass Transf. 102 (2016) 944–958.
- [37] S. Tao, Q. He, S.M. Huang, B.M. Chen, A non-iterative direct-forcing immersed boundary method for thermal discrete unified gas kinetic scheme with Dirichlet boundary conditions, Int. J. Heat Mass Transf. 137 (2019) 476–488.
- [38] Y.T. Bo, P. Wang, Z.L. Guo, L.P. Wang, Dugks simulations of three-dimensional Taylor-Green vortex flow and turbulent channel flow, Comput. Fluids 155 (2017) 9–21.
- [39] E.M. Shakhov, Generalization of the Krook kinetic relaxation equation, Fluid Dyn. 3 (1968) 142–145.
- [40] L.H. Holway, New statistical model for kinetic theory: method of construction, Phys. Fluids 9 (1968) 142–145.
- [41] K. Xu, A gas-kinetic BGK scheme for the Navier-Stokes equations and its connection with artificial dissipation and Godunov method, J. Comput. Phys. 171 (2001) 289–335.
- [42] X.W. Shan, X.F. Yuan, H.D. Chen, Kinetic theory representation of hydrodynamics: a way beyond the Navier-Stokes equation, J. Fluid Mech. 550 (2006) 413–441.
- [43] T. Chen, L.P. Wang, J. Lai, S.Y. Chen, Inverse design of mesoscopic models for compressible flow using the Chapman-Enskog analysis, Adv. Aerodyn. 3 (2021) 5.
- [44] T. Fusegi, J.M. Hyun, K. Kuwahara, B. Farouk, A numerical study of three-dimensional natural convection in a differentially heated cubical enclosure, Int. J. Heat Mass Transf. 34 (1991) 1543–1557.
- [45] S.M. Bilski, J.R. Lloyd, K.T. Yang, An experimental investigation of the laminar natural convection velocity in square and partitioned enclosures, Int. J. Heat Transf. 4 (1986) 1513–1518.
- [46] G. de Vahl Davis, I.P. Jones, Natural convection in a square cavity: a comparison exercise, Int. J. Numer. Methods Fluids 3 (1983) 227-248.
- [47] E. Tric, G. Labrosse, M. Betrouni, A first incursion into the three-dimensional structure of natural convection of air in a differentially heated cubic cavity, from accurate numerical solutions, Int. J. Heat Mass Transf. 43 (2000) 4043–4056.
- [48] M. Darbandi, S.F. Hosseinizadeh, Numerical study of natural convection in vertical enclosures using a novel non-Boussinesq algorithm, Numer. Heat Transf., Part A 52 (2007) 849–873.
- [49] V. Heuveline, On higher-order mixed fem for low Mach number flows: application to a natural convection benchmark problem, Int. J. Numer. Methods Fluids 41 (2003) 1339–1356.
- [50] K. MacGranttan, S. Hostikka, R. McDermott, Fire dynamic simulator: technical reference guide: Volume 1: Mathematical model, NIST Special Publication 1018-5.
- [51] F.X. Trias, M. Soria, A. Oliva, C.D. Pérez-Segarra, Direct numerical simulations of two- and three-dimensional turbulent natural convection flows in a differentially heated cavity of aspect ratio 4, J. Fluid Mech. 586 (2007) 259–293.